Transportation Research Part C 123 (2021) 102991

Contents lists available at ScienceDirect

Transportation Research Part C

journal homepage: www.elsevier.com/locate/trc

Delayed Lagrangian continuum models for on-board traffic prediction

Tamás G. Molnár [a,*], Devesh Upadhyay [b], Michael Hopka [b], Michiel Van Nieuwstadt [b], Gábor Orosz [a,c]

[a] Department of Mechanical Engineering, University of Michigan, Ann Arbor, MI 48109, USA
[b] Ford Research and Innovation Center, Dearborn, MI 48124, USA
[c] Department of Civil and Environmental Engineering, University of Michigan, Ann Arbor, MI 48109, USA

ARTICLE INFO

Keywords:
Connected vehicles
V2X connectivity
Traffic dynamics
Traffic flow models
Time delay
Lagrangian frame

ABSTRACT

In this paper we build Lagrangian continuum traffic flow models that are able to utilize trajectory information transmitted between connected vehicles via vehicle-to-everything (V2X) connectivity. These models capture three important features of traffic flow: (i) the propagation of congestions in time, (ii) the propagation of congestions in space, (iii) the string instability (or stability) of traffic that is related to the amplification (or decay) of traffic waves. The proposed models have only three tunable parameters to capture these three features. One of these parameters is the time delay that models the actuator lag in vehicle dynamics, the reaction time of human drivers, and the communication and feedback delays of connected and automated vehicles. The proposed Lagrangian continuum traffic models with delays establish a framework for traffic prediction and control. On one hand, connected vehicles may use predictions about the future motion of neighboring vehicles or their own. On the other hand, the continuum nature of these models allows one to study the large-scale impact of connected vehicles on the traffic flow. This opens the path for Lagrangian (vehicle-based) traffic control that supplements existing Eulerian (location-based) traffic control techniques.

1. Introduction

Today transportation is undergoing a fast development due to emerging technologies in vehicle-to-everything (V2X) connectivity, such as vehicle-to-vehicle (V2V) and vehicle-to-infrastructure (V2I) communication, or connectivity with cyclists, pedestrians and other traffic participants. V2X connectivity is able to provide connected vehicles (CVs) valuable information about surrounding traffic that is not directly perceivable by on-board sensors (Orosz et al., 2017). Connectivity does not necessarily require automated control, it can serve both connected automated vehicles (CAVs) and connected human-driven vehicles (CHVs) (Ge et al., 2018). In this paper, we focus on applications of connectivity for passenger vehicles on highways via V2V and V2I communication.

In V2X communication the most common messages include the position and speed of connected vehicles, that are called Lagrangian data. In general, traffic data may characterize certain road locations or describe the motion of individual vehicles; we refer to the location-based information as *Eulerian* and to the vehicle-based one as *Lagrangian*. Previously, traffic measurements could rely on Eulerian data by counting vehicles at a certain road location via loop detectors or cameras (Orosz et al., 2010; Mehran et al., 2011; Yu et al., 2020). After the occurrence of GPS-capable devices such as smartphones, however, Lagrangian data became also

* Corresponding author.
E-mail addresses: molnart@umich.edu (T.G. Molnár), dupadhya@ford.com (D. Upadhyay), mhopka@ford.com (M. Hopka), mvannie1@ford.com (M. Van Nieuwstadt), orosz@umich.edu (G. Orosz).

https://doi.org/10.1016/j.trc.2021.102991
Received 12 December 2019; Received in revised form 2 November 2020; Accepted 19 January 2021

widely available (Work and Bayen, 2008; Herrera et al., 2010). Routing apps (e.g. Waze, Google Maps, Here Maps and TomTom) provide awareness about surrounding traffic by aggregating Lagrangian data from their users to produce Eulerian (location-based) traffic forecasts. While data aggregation typically causes a few minutes delay in the forecasts, V2X connectivity provides another way to obtain information directly, in real time and in a standardized manner.

These applications show that leveraging Lagrangian data is getting more and more relevant in transportation. Traffic models, which can also be categorized into Eulerian and Lagrangian ones (Laval and Leclercq, 2013), are essential tools to leverage data. Initially, Eulerian traffic models have been more popular (Lighthill and Whitham, 1955; Richards, 1956). Although they are more suited for handling Eulerian data, Eulerian models may also utilize Lagrangian data, for example via ensemble Kalman filtering (Work et al., 2008, 2009, 2010), Newtonian relaxation (Herrera and Bayen, 2010) or integration of traffic flow models with car following models (Delle Monache et al., 2019a). Yet, it is more natural to use Lagrangian data by Lagrangian models, which have proven to be efficient in traffic estimation using floating car data (Yuan et al., 2012, 2014). Lagrangian models are also more suited for describing heterogeneous traffic including different vehicles (cars or trucks, human-driven or automated, connected or non-connected vehicles), because heterogeneity is induced by vehicle diversity rather than location-dependency (van Wageningen-Kessels et al., 2010).

For the reasons above, this paper aims to construct Lagrangian traffic models that directly handle the Lagrangian data obtained from connectivity. This can be achieved by car following models or continuum traffic flow models (Orosz et al., 2010), where the former ones are typically used for a few vehicles and short time scales, while the latter facilitate the study of large-scale traffic patterns. This paper is dedicated to the larger scales and the continuum models. While continua give a more aggregate description of the traffic flow, they also make the eventual conversion of models and results to Eulerian frame easier, and they facilitate extension to multi-lane or multi-class traffic (van Wageningen-Kessels et al., 2010; Leclercq and Laval, 2009). Here we construct Lagrangian continuum models, which are able to capture the main characteristics of traffic flow while having a small number of parameters. In particular, we capture the propagation of traffic congestions in time and space, as well as their amplification or decay. One key ingredient of these models is the time delay, which may represent vehicle dynamics (i.e., the time a vehicle needs to reach a prescribed velocity or acceleration), the reaction time of human drivers, the feedback delays in automated vehicles, or the communication delays in connected vehicles; see Orosz et al. (2010) for more details on the role of delays in traffic. The introduction of delays into continuum models is nontrivial, there are only a few recent attempts in the literature (Ngoduy, 2014; Burger et al., 2018; Tordeux et al., 2018; Burger et al., 2019; Göttlich et al., 2020). Since the delays correspond to a certain vehicle, they are of Lagrangian nature. Therefore, it is natural to include them in Lagrangian models, while, as will be shown, it is more complicated to take them into account by Eulerian models. The novelty of our work from modeling perspective is the introduction of time delays into Lagrangian continuum models and providing their Eulerian equivalent.

As an application of Lagrangian models, we make predictions about the future motion of connected vehicles in congested traffic based on the information they receive through V2X connectivity. Such on-board Lagrangian predictions can be tailored to the needs of the CVs and allow them to avoid undesired future states in traffic. This supplements existing Eulerian prediction techniques (Min and Wynter, 2011; Loumiotis et al., 2018; Yin et al., 2018) that are efficient in anticipating traffic at specific locations but are less suited to trajectory prediction or to handling mixed traffic with delays. As a motivating example, we remark that applications in CAVs use information about the future motion of the preceding vehicle to improve energy efficiency and control performance (Dollar and Vahidi, 2018; Kamal et al., 2018). If the CAV receives trajectory data (such as position and speed) from a CV traveling farther ahead, it may use a Lagrangian prediction to estimate the future motion of its predecessor. This requires describing the traffic between the distant CV and the preceding vehicle, which can be achieved by the proposed Lagrangian model. While this example illustrates the benefits of Lagrangian continuum models, applications are not limited to this specific scenario. Apart from CAVs, for whom predictions are especially useful, CHVs may also forecast the future motion of surrounding vehicles or their own, while connected smart infrastructures can also provide predictions about when and where connected vehicles are expected to encounter a traffic jam and how much they shall decelerate (Jiang et al., 2021).

In addition to traffic forecasting, Lagrangian models may also help designing traffic control. In particular, traffic flow can be improved by controlling the motions of individual vehicles. This is called Lagrangian traffic control (Delle Monache et al., 2019b; Ersal et al., 2020; Avedisov et al., 2020), whose applications range from relying on a single CAV (Ge et al., 2018; Cui et al., 2017; Stern et al., 2018) to platoons and moving bottlenecks (Zhang and Orosz, 2016; Čičić and Johansson, 2018; Jin et al., 2018; Piacentini et al., 2018), while approaches to control design involve reinforcement learning (Wu et al., 2017; Kreidieh et al., 2018), optimal control (Ge and Orosz, 2017; Zheng et al., 2020), frequency domain analysis (Wu et al., 2018; Qin and Orosz, 2019; Molnár et al., 2018) and partial differential equation based designs (Yu et al., 2018; Bekiaris-Liberis and Delis, 2020), just to mention a few. Since the increasing penetration of automated vehicles significantly improves their large-scale effect on the traffic flow (Spiliopoulou et al., 2018), Lagrangian traffic control provides a viable alternative to supplement Eulerian traffic control approaches realized through the use of traffic lights or ramp metering at fixed locations (Karafyllis and Papageorgiou, 2018; Pasquale et al., 2018; Yu and Krstic, 2019). Control applications, therefore, further support the need for Lagrangian models and motivate our study.

The manuscript is organized as follows. Section 2 presents experiments conducted with connected vehicles on public roads to collect Lagrangian traffic data that will be used by traffic flow models. Section 3 gives an introduction to approaches and frameworks in traffic modeling, and highlights the differences between Lagrangian and Eulerian models. Delay free Lagrangian continuum models are constructed in Section 4 and the incorporation of time delays is discussed in Section 5. The performance of the models is demonstrated by numerical simulations and connectivity-based traffic prediction in Section 6. Conclusions and comments on future applications are summarized in Section 7.

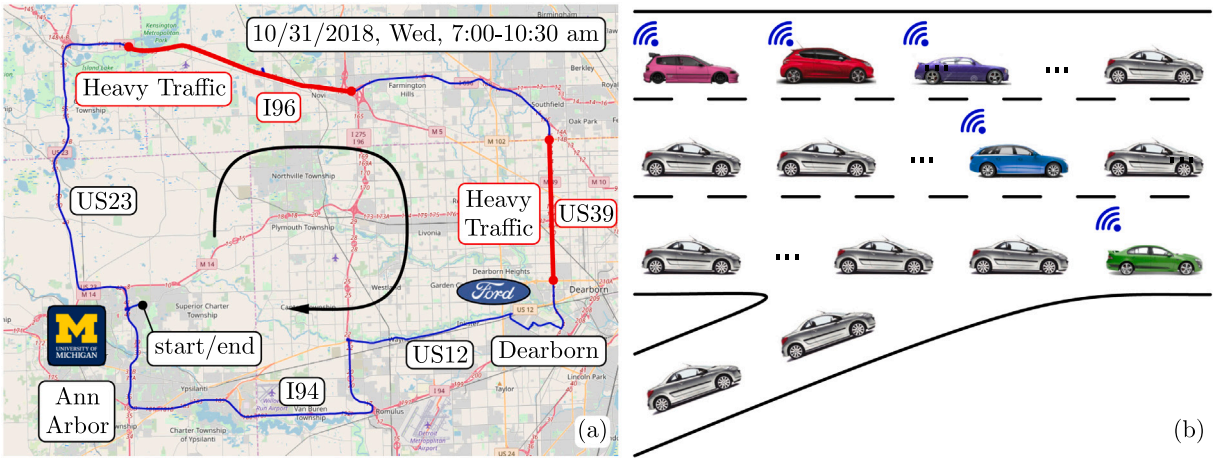

Fig. 1. (a) The route of the connected vehicles in the experimental Lagrangian traffic flow measurement. (b) Illustration of the experimental setup with five vehicles.

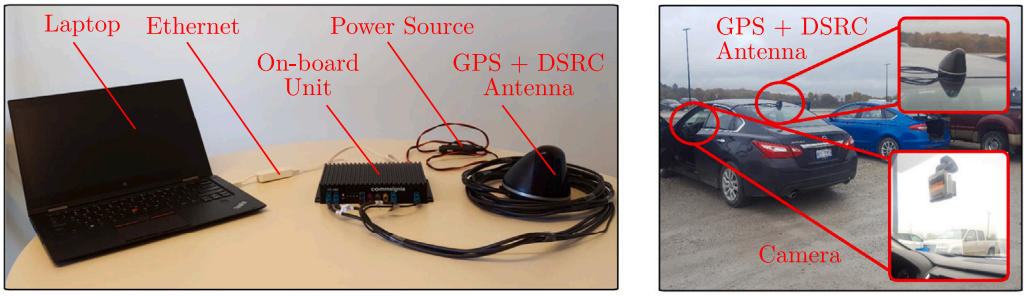

Fig. 2. The equipment utilized in the experimental Lagrangian traffic flow measurement.

2. Experimental traffic flow measurement using connected vehicles

As a motivation to this study, first we present experimental results. We describe the acquisition of Lagrangian traffic data, which is a fundamental requirement for any application in connected vehicles. We demonstrate the rich content of the Lagrangian data that were provided to the vehicles via connectivity, and we show what general features of the traffic flow can be extracted from the data. The data that we collected will be used as input for the Lagrangian continuum models in the rest of the paper.

2.1. Experimental setup

The experiment was conducted in collaboration with the Ford Research and Innovation Center. We drove five CHVs during the rush hour on the freeways in Michigan between Ann Arbor and Dearborn on a Wednesday morning as shown by the route highlighted in Fig. 1(a). Although the five vehicles started their journey at the same time and location, they were driven without the intention to closely follow each other and they did not intend to form a vehicle platoon. The vehicles were driven naturally, they were not necessarily occupying the same lane; see Fig. 1(b) for an illustration. We encountered two large traffic jams along the route (one on highway I96 and one on US39). By recording the trajectories of the five vehicles, we collected Lagrangian traffic data about these congestions.

In order to record the trajectory data, the equipment shown in Fig. 2 was used. GPS antennas were mounted on top of each vehicle, which allowed the acquisition of position, speed and heading angle signals. The vehicles were also equipped with on-board V2X units capable of dedicated short range communication (DSRC). These devices were transmitting basic safety messages (BSMs) that contain the GPS coordinates, speed and heading angle of individual vehicles. A laptop was connected to each DSRC device via Ethernet to record the BSMs. This way, five sets of data were collected: each dataset contains the information received by a given connected vehicle about the trajectories of all five connected vehicles.

Note that V2X allows data transmission within a range of up to a few hundred meters. Once the distance of the vehicles gets too large, the communication deteriorates and the transmitted data packets are lost. Apart from the distance, the rate of packet losses is also affected by vegetation, surrounding environment such as neighboring vehicles or objects that may occlude the communication, and additionally the weather conditions (e.g. rain, snow) may also modify the achievable range. In this experiment we used laptops

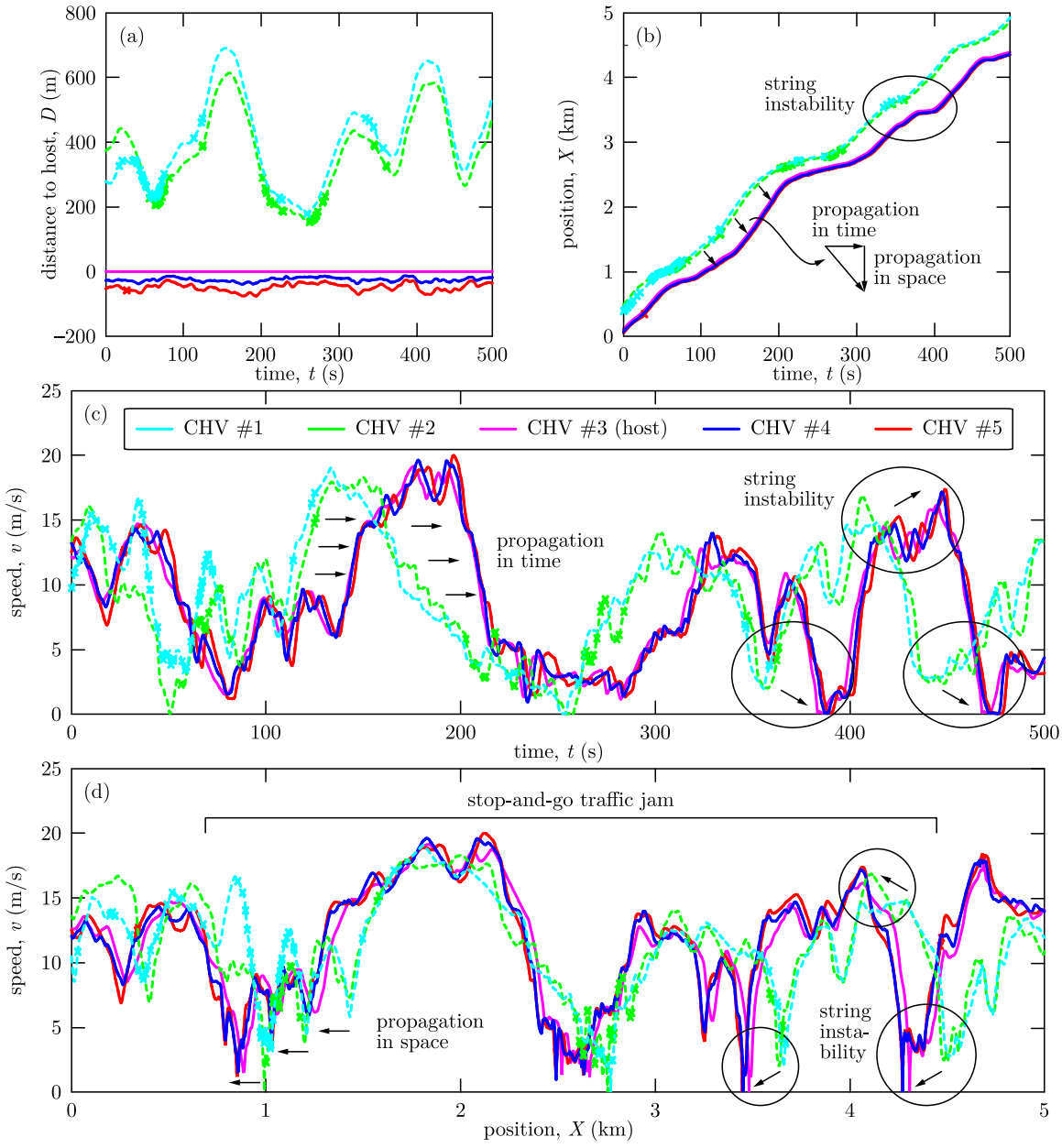

Fig. 3. Plot of the experimental data collected during a traffic jam, including (a) the distance of the five vehicles from a selected host vehicle as a function of time, (b) the position of the vehicles along the highway (i.e., the accumulated distance traveled by them) as a function of time, (c) the speed of the vehicles as a function of time, (d) the speed as a function of position. The trajectories of the five measured vehicles are indicated by five colors (cyan, green, magenta, blue, red). Solid lines show data available to the host vehicle, dashed lines show data not received by the host, and crosses indicate loss or reestablishment of communication with the host. (For interpretation of the references to color in this figure legend, the reader is referred to the web version of this article.)

on each vehicle to record the ground truth even when the vehicles were out of the communication range of the other connected vehicles. This allowed us to analyze the ground truth offline, after the experiments. However, in order to make on-board predictions for a specific connected vehicle, it is not necessary to record data by laptops on each of the other connected vehicles, only the V2X communication devices are required.

2.2. GPS data

The equipment discussed above enabled the collection of approximately three hours of Lagrangian traffic data from the perspective of five CHVs with a sampling time of 0.1 s. Fig. 3 presents the most significant results which were extracted from

the GPS data recorded over 500 s while traveling through the first traffic jam. The data related to the five CHVs is illustrated by five different colors. The results are plotted from an arbitrarily chosen, so-called host vehicle's point of view, that is, the inter-vehicular distances are measured relative to the host. Data received by the host is illustrated by solid lines. Dashed lines show the data that was not received by the host due to packet losses, but was measured on board of the other vehicles. Additionally, crosses are used to separate the solid lines from the dashed ones. This way, frequently interrupted communication is visualized by multiple crosses which show the time instants when a sequence of packet losses started or finished.

Fig. 3(a) shows the distance of the five CHVs from the host as a function of time (where the positive and negative signs indicate whether a vehicle is ahead of or behind the host). The solid lines (red and blue) indicate that the data is almost never subject to packet losses if it is sent from within 100 meters distance. However, above 200 meters distance, packet losses become more frequent and communication deteriorates, as shown by the dashed lines and crosses (green and cyan). The farthest distance where packets arrived from was about 500 meters (see the highest located crosses). Note, however, that these data were taken on a rainy day in heavily congested traffic conditions where many surrounding vehicles were blocking the communication. With clearer, less dense environment we were able to detect occasional packets even from about 1000 meters distance. For simplicity, we do not indicate packet losses in subsequent figures anymore, but we keep in mind the limited range of V2X connectivity.

Fig. 3(b) shows the position of the vehicles along the highway, i.e., the accumulated distance (arclength) traveled by them as a function of time. The trajectories of the five CHVs look qualitatively similar, but shifted in time and space. This time shift and spatial shift show the propagation of traffic congestions in time and space (Newell, 2002). A similar phenomenon is observable in Fig. 3(c,d), where the speed of the vehicles is plotted as a function of time and position, respectively. The speed fluctuations of the five CHVs are qualitatively similar, but shifted in time as highlighted in Fig. 3(c) and shifted in space as shown in Fig. 3(d). It is important to notice that the order of the five trajectories from left to right in Fig. 3(c) is the opposite to the one in Fig. 3(d). That is, the lead vehicle (cyan) meets the traffic jam the earliest in time (it is the leftmost in Fig. 3(c)), while it is able to travel the longest distance before reaching the congestions (it is the rightmost in Fig. 3(d)). This indicates the propagation of traffic congestions: vehicles that reach the traffic jam later in time encounter it earlier in space, since the traffic jam is propagating upstream (i.e., in the direction opposite to the traffic flow). By evaluating the spatial shift and the time shift between the speed signals, the jam speed was found to be around 5–6 m/s. The propagation of congestions in time and space is one of the key features to be captured by the Lagrangian traffic models introduced in Sections 4 and 5.

Although the speed profiles in Fig. 3(c,d) look similar qualitatively, there are significant quantitative differences between them. In particular, the speed fluctuations of the lead vehicles (cyan and green) are amplified by the tail vehicles (magenta, blue, red): vehicles upstream tend to decelerate more aggressively in congestions, which may even lead to stop-and-go motion (Orosz et al., 2010). In other words, perturbations amplify as propagating upstream along a string of vehicles, which is referred to as the string instability of the traffic flow (Swaroop and Hedrick, 1996; Ploeg et al., 2014; Besselink and Johansson, 2017; Feng et al., 2019). This phenomenon is also observable in Fig. 3(b) where the slope of the trajectories becomes smaller for vehicles upstream. String instability is often attributed to the reaction time of human drivers: when humans respond to perturbations with large delay (i.e., react to decelerations too late), they tend to amplify them (decelerate more). The string instability phenomenon is another key feature that is captured by the models in Section 5, where time delays play essential role.

2.3. Camera data

Apart from GPS and V2X, the vehicles were also equipped with cameras on their windshield to record the ground truth about their environment; see Fig. 2. The camera data contain additional pieces of information, which are not directly available from the GPS signals: the number of lanes on the road, the lanes in which the vehicles are traveling and the lane changes; the location of on- and off-ramps along the highway; bridges, tunnels and overpasses (where the GPS signal may be lost); and surrounding vehicles. Note, however, that these data are restricted to the immediate surroundings of the vehicles, while V2X connectivity may provide information from beyond the line of sight.

Fig. 1(b) illustrates the lane of the five CHVs and their location relative to each other during the second traffic jam we encountered as reconstructed from the camera data. Furthermore, Fig. 4 shows the corresponding speed profiles together with information about the environment. All lanes were congested according to the figure, and speed fluctuations are qualitatively similar regardless the choice of the lane under such conditions. This means that utilizing Lagrangian data provided by V2X connectivity can be useful even if the data come from a vehicle in another lane. The location of on- and off-ramps (which were on the right side of the road) are also indicated by symbols ▲ and ▼, respectively. Around on-ramps vehicles need to decelerate since others are entering the highway. This deceleration may trigger a traffic wave, which then propagates upstream. For example, the lead vehicle (green) decelerates at the first on-ramp in Fig. 4, while the following vehicles decelerate even before reaching the on-ramp. This indicates that perturbations propagate upstream, and it is observable for the second on-ramp as well. However, once formed, traffic congestions behave dynamically: they move, amplify and decay along the highway. Thus, vehicles may decelerate even without the presence of an on-ramp, as shown on the right of Fig. 4.

In what follows, we revisit the basic approaches for traffic flow modeling and build Lagrangian models to predict the above mentioned experimental observations, including the temporal and spatial shifts of speed fluctuations and the string instability phenomenon. These models provide Lagrangian traffic predictions that CVs can directly utilize to improve their performance, and also allow us to study the effects of CAVs on the traffic flow.

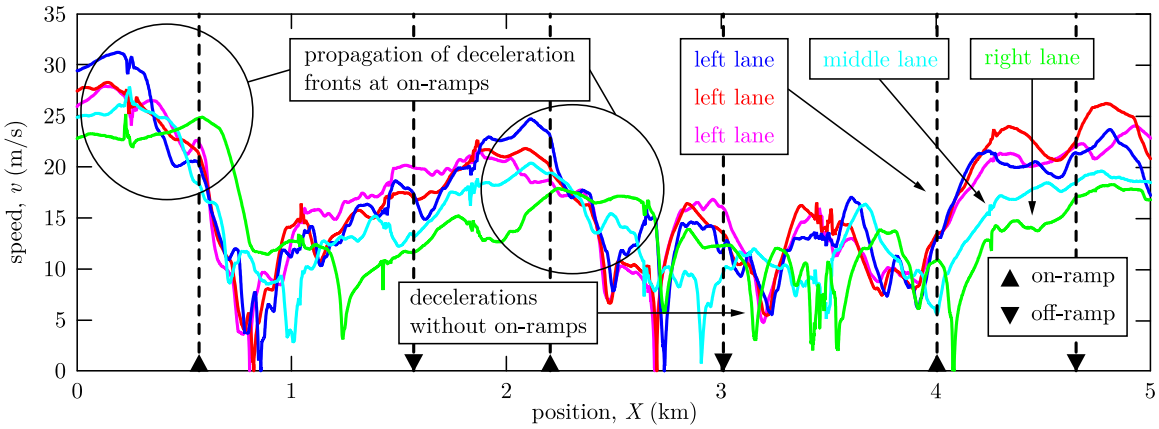

Fig. 4. Experimental speed data as a function of vehicular position during a traffic jam. The speeds of the five measured vehicles are indicated by color (green, cyan, blue, red, magenta). The figure also shows information reconstructed from camera data: the lane of the vehicles and the location of on-ramps (▲) and off-ramps (▼). (For interpretation of the references to color in this figure legend, the reader is referred to the web version of this article.)

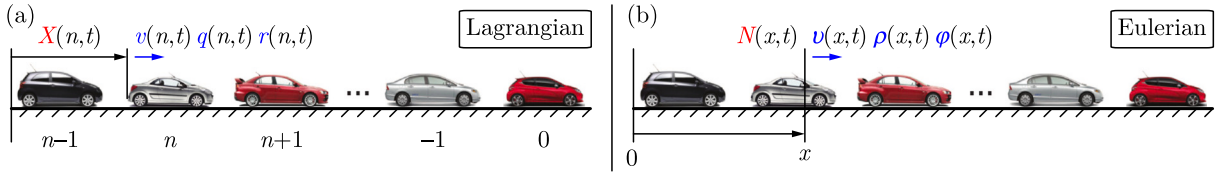

Fig. 5. Illustration of (a) the Lagrangian and (b) the Eulerian framework for traffic flow description.

3. Approaches for traffic flow description

In general, techniques for traffic flow modeling can be categorized into *microscopic* and *macroscopic* approaches. Microscopic models typically deal with a few vehicles over a time scale of seconds. They trace the motion of a discrete, integer number of individual vehicles and use ordinary or delay differential equations to describe their dynamics. Macroscopic models, on the other hand, are usually accommodated to study traffic flows over hours in a road fixed frame. They typically describe traffic flow as continuum via partial differential equations. That is, the term "microscopic" usually refers to Lagrangian discrete car following models, whereas "macroscopic" typically indicates Eulerian continuum traffic flow models. Bridging the two approaches and predicting traffic over the time scale of minutes is still an open question. This research targets this problem. We focus mainly on continuum models and investigate the simple scenario of one-directional highway traffic without considering the effect of overtaking.

As summarized in Laval and Leclercq (2013), the flow of traffic can be imagined as evolution in a three dimensional space of variables: time t, location x, and the index n of vehicles. These quantities are illustrated in Fig. 5. Time can be measured from any chosen initial instant $t = 0$. The location x is measured along the highway such that it increases downstream (i.e., in the direction where vehicles are heading) and $x = 0$ can be chosen at any arbitrary start location of interest. To distinguish each participating vehicle in traffic, an index n is associated to them, which increases downstream and $n = 0$ can be chosen for any arbitrary lead vehicle. We remark that continuum models do not restrict to integer numbers of vehicles, the vehicle index n can be non-integer as well. A quantity at a non-integer vehicle index represents interpolation between the integer labeled physical vehicles.

3.1. Independent variables

In order to describe the traffic flow, one can choose two of the three fundamental quantities (time t, location x and vehicle index n) as independent variables: (n,t), (x,t) or (n,x). Note that we denote independent variables by lowercase letters. Then the remaining one fundamental quantity can be chosen as dependent variable, which we denote by an uppercase letter: X, N or T, respectively. This implies three different frameworks for traffic description.

The first framework is called *Lagrangian*. Here the motion of individual vehicles is traced to describe the traffic flow as a function of vehicle index n and time t; see Fig. 5(a). The most fundamental quantity of this framework is the vehicular *position* $X(n,t)$ (measured in m). This can be measured directly by equipping vehicles with GPS, and it is a monotonically increasing function of t and a strictly monotonically increasing function of n (since the vehicle index increases downstream). The trajectory $X(n,t)$ is illustrated as a family of curves in the (t,X) plane in Fig. 6. The slope of these curves represents the speed of vehicles, the horizontal distance between two curves is the time between two vehicles passing the same location, and the vertical distance is the physical distance of two vehicles at a given time.

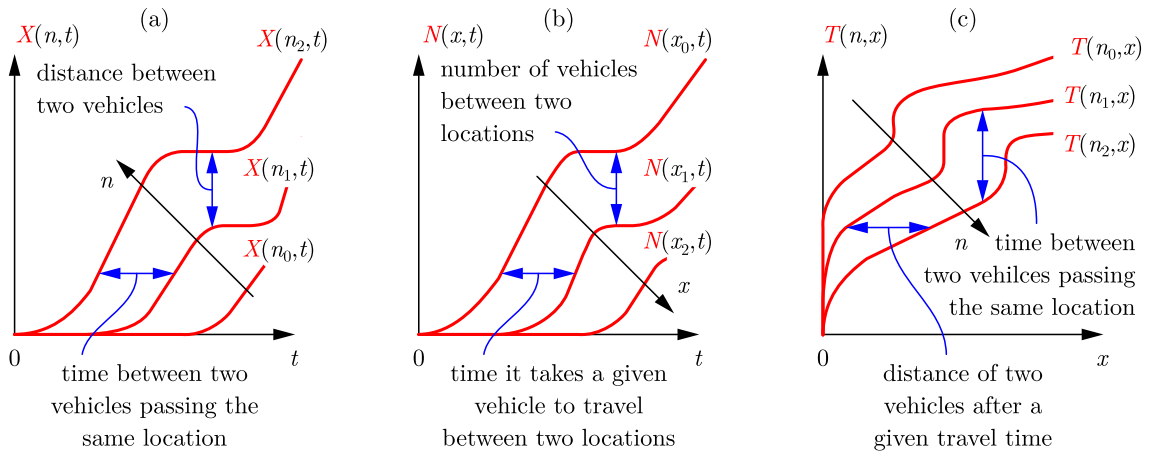

Fig. 6. Qualitative picture of (a) the vehicular position, (b) the cumulative flow, and (c) the travel time.

In the second, *Eulerian* framework a certain cross section of the road is selected for observation and traffic measures are formulated as a function of location x and time t; see Fig. 5(b). The fundamental quantity of this framework is the *cumulative flow* $N(x,t)$ (measured in vehicles). This indicates the number of vehicles that reach location x by time t (Laval and Leclercq, 2013; Newell, 1993), and it is a monotonically increasing function of t and a strictly monotonically decreasing function of x (since less vehicles reach locations farther along the road). Note that opposite to the vehicle index n, the cumulative flow decreases downstream. The cumulative flow $N(x,t)$ is shown by a family of curves in the (t,N) plane in Fig. 6. The slope of these curves is the traffic flux, the horizontal distance between two curves is the time a given vehicle needs to travel between two locations, and the vertical distance is the number of vehicles between two locations.

The third framework describes traffic as a function of vehicle index n and location x. This framework gives the *travel time* $T(n,x)$ (measured in s) needed for vehicle n to reach location x, and it is a strictly monotonically decreasing function of n and a strictly monotonically increasing function of x (if the vehicles are in motion). However, this framework is not able to address situations where vehicles stop on the road and multiple travel times correspond to a single vehicle index and location. Strictly speaking, $T(n,x)$ is not a function in such cases, thus we refrain from using this framework in the rest of the paper. Still, for the sake of completeness, the travel time $T(n,x)$ is shown as a family of curves in the (x,T) plane in Fig. 6. The slope of these curves is the pace (the inverse of the speed), the horizontal distance between two curves is the physical distance of vehicles after a given travel time, and the vertical distance is the time between two vehicles passing the same location. Further details on this framework can be found in Laval and Leclercq (2013).

From this point on, we restrict ourselves to the Lagrangian and Eulerian frameworks shown in Fig. 5. Quantities in the Eulerian framework can be converted to Lagrangian ones by substituting location x with the position $X(n,t)$. Meanwhile, the Lagrangian to Eulerian transformation is achieved by the substitution of the vehicle index n with the negative cumulative flow $-N(x,t)$, where the negative sign comes from the convention that the vehicle index increases downstream (while the cumulative flow decreases downstream). This leads to the identities

$$\begin{aligned} x &= X(-N(x,t),t)\,, \\ n &= -N(X(n,t),t)\,. \end{aligned} \tag{1}$$

3.2. Dependent variables

Apart from the position $X(n,t)$ and the cumulative flow $N(x,t)$, other important traffic measures also exist, such as the vehicular *speed* (measured in m/s), the traffic *density* (measured in vehicles/m) and the traffic *flux* (measured in vehicles/s). Speed is the distance traveled over unit time, density is the number of vehicles located on a highway segment of unit length, while flux is the number of vehicles passing a location over unit time. For the sake of clarity, we denote these quantities by Roman letters in Lagrangian and by Greek letters in Eulerian framework: speed as $v(n,t)$ or $\upsilon(x,t)$, density as $r(n,t)$ or $\rho(x,t)$ and flux as $q(n,t)$ or $\varphi(x,t)$, respectively. The relation between Lagrangian and Eulerian traffic measures is given by

$$\begin{aligned} v(n,t) &= \upsilon(X(n,t),t)\,, \\ r(n,t) &= \rho(X(n,t),t)\,, \\ q(n,t) &= \varphi(X(n,t),t)\,, \end{aligned} \tag{2}$$

and

$$\begin{aligned} \upsilon(x,t) &= v(-N(x,t),t)\,, \\ \rho(x,t) &= r(-N(x,t),t)\,, \\ \varphi(x,t) &= q(-N(x,t),t)\,, \end{aligned} \tag{3}$$

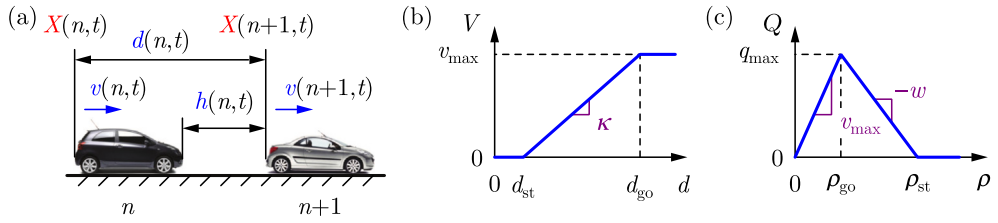

Fig. 7. Illustration of (a) the car following model, (b) the range policy, and (c) the corresponding fundamental diagram.

while the flux is the product of speed and density

$$\begin{aligned} q(n,t) &= r(n,t)v(n,t)\,, \\ \varphi(x,t) &= \rho(x,t)v(x,t)\,. \end{aligned} \tag{4}$$

Eq. (4) implies that only two quantities are independent in the triplet of speed, density and flux. Therefore, irrespective of using Lagrangian or Eulerian frameworks, one can choose a pair of dependent variables from this triplet. Alternatively, it is sufficient to choose a single dependent variable if a fundamental quantity – position or cumulative flow – is used. The reason behind this is that speed, density and flux originate from the derivatives of position and cumulative flow (Laval and Leclercq, 2013). The derivative of position with respect to time is speed and with respect to vehicle index is inverse density:

$$\begin{aligned} \partial_t X(n,t) &= v(n,t)\,, \\ \partial_n X(n,t) &= \frac{1}{r(n,t)}\,, \end{aligned} \tag{5}$$

while the derivative of cumulative flow with respect to time is flux and with respect to position is negative density:

$$\begin{aligned} \partial_t N(x,t) &= \varphi(x,t)\,, \\ \partial_x N(x,t) &= -\rho(x,t)\,. \end{aligned} \tag{6}$$

Equivalently, in integral form we can write

$$X(n,t) = X(n,0) + \int_0^t v(n,\tilde{t})\mathrm{d}\tilde{t} = X(0,t) + \int_0^n \frac{1}{r(\tilde{n},t)}\mathrm{d}\tilde{n}\,, \tag{7}$$

$$N(x,t) = N(x,0) + \int_0^t \varphi(x,\tilde{t})\mathrm{d}\tilde{t} = N(0,t) - \int_0^x \rho(\tilde{x},t)\mathrm{d}\tilde{x}\,, \tag{8}$$

where the four integrals represent the distance traveled by vehicle n over $[0,t]$, the distance between vehicle 0 and n at time t, the number of vehicles passing location x over $[0,t]$ and the number of vehicles between locations 0 and x at time t, respectively.

4. Delay free kinematic traffic flow models

In what follows, we restrict ourselves to the simplest, so-called kinematic models, which are formulated at the level of speed. For models constructed at the acceleration level, the reader is referred to Orosz et al. (2010) and the references therein. In Section 4 we discuss delay free models, then Section 5 addresses time delays originating from vehicle dynamics, driver reaction time, feedback loops or communication. We show both discrete models and the corresponding continuum traffic description by following our previous work in Molnár et al. (2019). Note that discrete car following models are well suited for directly utilizing trajectory data from V2X connectivity, however, simulating each individual vehicle separately may make them computationally expensive. Meanwhile, continuum models treat traffic as a flow without distinguishing each individual vehicle, and they give an aggregated description of traffic. Thus, we focus more on continuum models, and we highlight the relevance of the Lagrangian formulation of these models in applications related to CVs.

4.1. An approach for constructing continuum models

Discrete traffic models – that consider an integer number of vehicles – are naturally formulated in Lagrangian framework, since they are discrete in the vehicle index n. For example, typical car following models use the trajectory $X(n+1,t)$ of a lead vehicle $n+1$ and the trajectory $X(n,t)$ of a follower vehicle n; see the illustration in Fig. 7(a). Thus, the resulting equations involve a unit shift (delay) in the argument n owing to the term $X(n+1,t)$. In order to construct continuum models corresponding to discrete ones, this unit shift should be eliminated and derivatives with respect to the vehicle index n should be used. For more details on the relation between discrete and continuum models, see Jin (2016).

A potential approach to transition from discrete to continuum models is to expand the follower's position $X(n,t)$ with respect to its first argument around the leader's position $X(n+1,t)$ as

$$X(n,t) = \sum_{m=0}^{M_X} \frac{(-1)^m}{m!}\partial_n^m X(n+1,t) = X(n+1,t) - \partial_n X(n+1,t) + \frac{1}{2}\partial_{nn} X(n+1,t) - \cdots + \frac{(-1)^{M_X}}{M_X!}\partial_n^{M_X} X(n+1,t)\,, \tag{9}$$

where ∂_n^m denotes the mth derivative with respect to n and M_X is the order of Taylor expansion. Note that physically (9) establishes the relation between the distance $d(n,t) = X(n+1,t) - X(n,t)$ and the inverse $\partial_n X(n,t)$ of the density $r(n,t)$; see Berg et al. (2000) for a study on this topic. Similarly, Taylor expansion can also be done for the speed up to order M_v:

$$\partial_t X(n,t) = \sum_{m=0}^{M_v} \frac{(-1)^m}{m!} \partial_n^m \partial_t X(n+1,t) = \partial_t X(n+1,t) - \partial_{nt} X(n+1,t) + \frac{1}{2}\partial_{nnt} X(n+1,t) - \cdots + \frac{(-1)^{M_v}}{M_v!}\partial_n^{M_v}\partial_t X(n+1,t)\,. \tag{10}$$

Hereafter, we use the expansions (9)–(10) to build Lagrangian continuum models from discrete ones, then we drive the constructed models with the experimental data to make Lagrangian traffic predictions.

4.2. Continuum models constructed from a benchmark discrete model

Below we consider a simple discrete model as a basis to construct continuum traffic flow models via the approach discussed above. As one of the most essential kinematic traffic flow models, we consider Newell's model (Newell, 2002, 1961). This model focuses on a leader–follower pair of vehicles shown in Fig. 7. It assumes that vehicle n controls its speed $v(n,t)$ based on the headway $h(n,t)$ or, equivalently, the distance $d(n,t)$ from its predecessor $n+1$. This can be given in the form of the ordinary differential equation (ODE)

$$\partial_t X(n,t) = V(X(n+1,t) - X(n,t))\,, \tag{11}$$

where the function V defines the distance–velocity relationship, which is also referred to as the range policy in the rest of the paper. Note that (11) assumes identical vehicles with identical range policies (same V for each n), but it can easily be extended to heterogeneous traffic (with an n-dependent range policy).

The range policy is illustrated in Fig. 7(b). Accordingly, vehicle n needs to stop below a safety distance d_{st} and the assigned speed is zero. Above a certain distance d_{go}, the vehicle shall travel with the speed limit $v_{\max}$. Between d_{st} and d_{go}, the speed monotonically increases against the distance: the farther the vehicles move away from each other, the faster they shall travel. For example, if this monotonically increasing tendency is linear, the range policy becomes

$$V(d) = \begin{cases} 0 & \text{if} \quad d \le d_{\mathrm{st}}\,, \\ \kappa(d - d_{\mathrm{st}}) & \text{if} \quad d_{\mathrm{st}} < d < d_{\mathrm{go}}\,, \\ v_{\max} & \text{if} \quad d_{\mathrm{go}} \le d\,, \end{cases} \tag{12}$$

where $d_{\mathrm{go}} = d_{\mathrm{st}} + v_{\max}/\kappa$, and κ denotes the slope of the range policy; see the illustration in Fig. 7(b). Note that $1/\kappa$ can also be interpreted as the time gap between the vehicles if d_{st} is equal to the length of the vehicles.

Now let us approximate the discrete model (11) with a continuum one via the expansions (9)–(10). Substitution into (11) and shifting the index $n+1$ to n leads to the partial differential equation (PDE)

$$\sum_{m=0}^{M_v} \frac{(-1)^m}{m!} \partial_n^m \partial_t X(n,t) = V\left(-\sum_{m=1}^{M_X} \frac{(-1)^m}{m!} \partial_n^m X(n,t)\right). \tag{13}$$

Below we discuss an important special case of this model and then give extensions to models with time delay.

4.3. A special case: the Lighthill–Whitham–Richards model

The simplest, lowest order continuum approximation of (11) is obtained from (13) by substituting $M_v = 0$ and $M_X = 1$. This leads to the continuum model

$$\partial_t X(n,t) = V(\partial_n X(n,t))\,. \tag{14}$$

If the middle, linear part of the range policy (12) is effective for all n and t, this equation is an affine PDE. Furthermore, if the initial condition is the equidistant spacing $X(n,0) = X(0,n/\kappa) + nd_{\mathrm{st}}$, the solution is the traveling wave

$$X(n,t) = X\left(0, t + \frac{n}{\kappa}\right) + nd_{st}\,, \tag{15}$$

which can also be obtained from Newell's model in Newell (2002). This implies shifted vehicle trajectories (similarly to the ones observed in Fig. 3(a)) with time shift $1/\kappa$ and spatial shift d_{st}, while the corresponding wave speed is $w = \kappa d_{\mathrm{st}}$.

Notice that the difference of positions in (11), which represents inter-vehicular distance, is replaced by a position derivative in (14), which is related to traffic density according to (5). Therefore, model (14) can also be formulated as a speed–density relationship

$$\partial_t X(n,t) = \mathcal{V}\left(\frac{1}{\partial_n X(n,t)}\right), \tag{16}$$

where the function $\mathcal{V}(r) = V(1/r)$ describes that the denser the traffic gets, the slower the vehicles travel. Let us supplement model (16) with the identity

$$\partial_{tn} X(n,t) - \partial_{nt} X(n,t) = 0\,. \tag{17}$$

Hereinafter, we use this identity to show that (16)–(17) is in fact the Lagrangian equivalent of the well known Lighthill–Whitham–Richards (LWR) model (Lighthill and Whitham, 1955; Richards, 1956). The various forms of the LWR model, including the Lagrangian (16), can also be found in Leclercq et al. (2007).

To show the equivalence, we formulate the model in terms of Lagrangian speed $v(n,t)$ and density $r(n,t)$ by substituting (5) into (16) and (17):

$$\begin{aligned} \partial_t \frac{1}{r(n,t)} - \partial_n v(n,t) = 0\,, \\ v(n,t) = \mathcal{V}(r(n,t))\,, \end{aligned} \tag{18}$$

see also in Leclercq et al. (2007) and Aw et al. (2002). The first row of (18) can be interpreted as a conservation law for the number of vehicles participating in traffic, while the second row tells how the traffic is modeled.

Now let us represent the model in Eulerian framework. We substitute (2) into (18), carry out differentiations according to the chain rule, use (5), and finally substitute $x = X(n,t)$. This leads to the classical Eulerian form of the LWR model using speed $v(x,t)$ and density $\rho(x,t)$, that is,

$$\begin{aligned} \partial_t \rho(x,t) + \partial_x(\rho(x,t)v(x,t)) = 0\,, \\ v(x,t) = \mathcal{V}(\rho(x,t))\,, \end{aligned} \tag{19}$$

or by using flux $\varphi(x,t)$ and density $\rho(x,t)$ it becomes

$$\begin{aligned} \partial_t \rho(x,t) + \partial_x \varphi(x,t) = 0\,, \\ \varphi(x,t) = \rho(x,t)\mathcal{V}(\rho(x,t))\,. \end{aligned} \tag{20}$$

The first row of (20) describes the conservation of vehicles on the road, which is analogous to the conservation of mass in fluid dynamics. The second row specifies the flux–density relation via the function $\mathcal{Q}(\rho) := \rho\mathcal{V}(\rho) = \rho V(1/\rho)$. The relation corresponding to (12) reads

$$\mathcal{Q}(\rho) = \begin{cases} 0 & \text{if} \quad \rho_{\text{st}} \le \rho\,, \\ \kappa\left(1 - \dfrac{\rho}{\rho_{\text{st}}}\right) & \text{if} \quad \rho_{\text{go}} < \rho < \rho_{\text{st}}\,, \\ \rho v_{\max} & \text{if} \quad \rho \le \rho_{\text{go}}\,, \end{cases} \tag{21}$$

where $\rho_{\text{st}} = 1/d_{\text{st}}$ and $\rho_{\text{go}} = 1/d_{\text{go}}$. Function $\mathcal{Q}(\rho)$ is illustrated by the well known fundamental diagram in Fig. 7(c). Note that the slope $w = \kappa/\rho_{\text{st}} = \kappa d_{\text{st}}$ can also be interpreted as the speed of the traveling wave solutions of (20), that is, the speed of congestion waves in the traffic flow.

Finally, the LWR model can also be formulated in Eulerian framework using the cumulative flow $N(x,t)$. By substituting (6) into (20) we obtain

$$\begin{aligned} -\partial_{tx} N(x,t) + \partial_{xt} N(x,t) = 0\,, \\ \partial_t N(x,t) = -\partial_x N(x,t)\mathcal{V}(-\partial_x N(x,t))\,, \end{aligned} \tag{22}$$

which can also be found in Newell (1993) and Leclercq et al. (2007). Similarly to (17), the first row of (22) is an identity, which implies that the definitions (5) and (6) of the densities $r(n,t)$ and $\rho(x,t)$ ensure the fulfillment of the conservation law of vehicles.

The equivalence of (20) with (16)–(17) shows that the LWR model is in fact related to Newell's model (11) by a low order Taylor expansion ($M_X = 1$, $M_v = 0$) in (13). Higher order expansions ($M_X > 1$, $M_v > 0$) are also possible, see also Berg's work (Berg et al., 2000) for a similar approach. The higher order terms can be considered as source terms in the LWR model. The literature on continuum traffic flow models contains various attempts to specify reasonable source terms, which lead to sophisticated models capturing more details about the evolution of traffic flow (Daganzo, 1994; Aw and Rascle, 2000; Zhang, 2002; Garavello and Piccoli, 2006). However, the construction and physical explanation of these source terms is nontrivial. In this paper, these terms were derived from the approximation (Taylor expansion) of a discrete model. Below we show that these higher order terms become significant when time delays are incorporated into the equations. Before dealing with the delays, we demonstrate the performance of the delay free models and show why delays are necessary to include.

4.4. Numerical simulations utilizing Lagrangian traffic data

We conducted numerical simulations for the LWR model that was driven by the Lagrangian traffic data we had collected during our experiment. The results are summarized in Fig. 8. Panel (a) shows the speed $v(n,t)$ of the vehicles, and panel (b) shows the distance $D(n,t) = X(0,t) - X(n,t)$ of the vehicles from the lead vehicle (thick cyan curve) whose motion was used to drive the model. The experimental data are indicated by thick lines and the simulation results are shown by thin lines. Since we drove multiple vehicles in the traffic flow, we can compare their measured trajectories to the simulated ones. If the model was a perfect representation of reality, four of the simulated results (thin gray lines) would coincide with the four measured follower trajectories (thick green, magenta, blue, red).

We used the Lagrangian form (14) of the LWR model for the simulations, since it directly includes the measurement data as boundary condition. Considering trajectory data is also possible in the Eulerian frame, however, the underlying mathematics

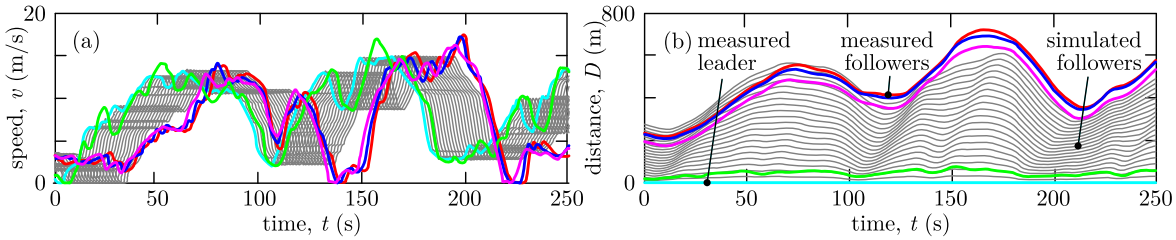

Fig. 8. The results of numerical simulations (thin) using the LWR model (14) compared to the experimental Lagrangian traffic data (thick): (a) the speed of vehicles, (b) their distance from the lead vehicle (cyan). The parameters of the model are $d_{st} = 10\,\mathrm{m}$, $v_{max} = 30\,\mathrm{m/s}$ and $1/\kappa = 1.5\,\mathrm{s}$. (For interpretation of the references to color in this figure legend, the reader is referred to the web version of this article.)

become more complicated due to the occurrence of internal boundary conditions (Claudel and Bayen, 2010a,b). Here we selected the trajectory $X_0(t)$ of the measured lead vehicle (thick cyan) and imposed it as boundary condition on the Lagrangian model: $X(0,t) = X_0(t)$. Then we simulated the trajectory of 20 follower vehicles ($n \in [-20, 0]$) with the initial condition $X(n,0) = X(0,0) + nd_0$ where d_0 is the uniform initial spacing between the simulated vehicles. We selected $d_0 = d_{st}$, since we used experimental data where vehicles start from standstill. We assumed the parameter values $d_{st} = 10\,\mathrm{m}$, $v_{max} = 30\,\mathrm{m/s}$ and $1/\kappa = 1.5\,\mathrm{s}$. We discretized (14) by the Lax–Wendroff scheme (Press et al., 1992) using a time step $\Delta t = 0.1\,\mathrm{s}$ and a step of $\Delta n = 0.1$ in the vehicle index. Notice that trajectories corresponding to non-integer vehicle indices were also computed but they are not plotted in Fig. 8.

Fig. 8(a) shows that the LWR model outputs repeated speed patterns similarly to the traveling wave solutions (15), i.e., it is able to capture the propagation of traffic congestions in time. Their propagation in space is also reproduced by the model, since the distance of the simulated vehicles in Fig. 8(b) resembles the measured inter-vehicular distances. Note that the distance between the vehicles is affected by both the spatial shift d_{st} and the distance that the vehicles travel over the time shift $1/\kappa$. Still, the model is simple and allows capturing two features – the propagation of congestions in time and space – using only two tunable parameters: κ and d_{st}.

Although the propagation of speed fluctuations can be reproduced, the model is not able to capture amplifying or decaying speed fluctuations, i.e., string unstable or string stable behavior. The amplitude of speed fluctuations is the same for each vehicle; see Fig. 8(a). This is due to the hyperbolic nature of the governing PDE (Laval and Leclercq, 2013), whose spectrum and string stability properties are further discussed in Appendix. In what follows, our aim is to capture string stability properties with the addition of a single tunable parameter to the model: the time delay.

5. Kinematic traffic flow models with time delay

Models (11) and (13) of Section 4 address the relation between the instantaneous values of certain traffic measures. However, human drivers tend to react to rather the past state of traffic than the instantaneous state due to their reaction time (Orosz et al., 2010). This can be modeled by time delays in the governing equations. Delays can also describe the dead time in the feedback loops of automated vehicles, communication latency in connected vehicles, or even the vehicle dynamics, i.e., the fact that vehicles need a certain time to reach a desired speed. Hereinafter we discuss how to incorporate time delays into the models introduced in Section 4.

5.1. Construction of continuum models with delay

The delayed counterpart of Newell's discrete model (11) can be found in Igarashi et al. (2001). Accordingly, vehicle n adjusts its speed $v(n,t)$ based on the past value $d(n, t-\tau)$ of the distance from its predecessor. This leads to the delay differential equation (DDE)

$$\partial_t X(n,t) = V(X(n+1, t-\tau) - X(n,t-\tau)), \tag{23}$$

where τ denotes the time delay. Since this delay corresponds to a certain vehicle, it is Lagrangian delay. That is, the vehicle index in the first argument of X is not affected by the delay, it is the same as in (11). Model (23) involves a constant delay τ, but it can be extended to the case where the delay $\tau(n,t)$ depends on the vehicle index n (to represent the heterogeneity of traffic flow; see Section 5.4) and on time t.

The continuum counterpart of the discrete time delay model (23) can be constructed similarly to Section 4, by substituting (9)–(10) into (23). This leads to the partial delay differential equation (PDDE)

$$\sum_{m=0}^{M_v} \frac{(-1)^m}{m!} \partial_n^m \partial_t X(n,t) = V\left(-\sum_{m=1}^{M_X} \frac{(-1)^m}{m!} \partial_n^m X(n, t-\tau) \right), \tag{24}$$

cf. (13).

5.2. Delayed Lighthill–Whitham–Richards model

Again let us consider the lowest order expansion ($M_X = 1,\ M_v = 0$) as a special case, which leads to the delayed LWR model. We use this example to demonstrate two important conclusions of this paper. On one hand, we highlight that the formulation of delayed continuum models is much more complicated in the Eulerian framework than in the Lagrangian one, since the delays are fundamentally of Lagrangian nature. On the other hand, we show that simply adding the delay to the LWR model leads to string unstable results regardless the value of the delay, and higher order terms are also required during the construction of delayed continuum models.

Substituting $M_X = 1,\ M_v = 0$ into (24) gives the delayed LWR model in the form

$$\partial_t X(n,t) = V(\partial_n X(n,t-\tau))\,, \tag{25}$$

cf. (14). This model, supplemented by the identity (17), can be transformed into various forms depending on the choice of dependent and independent variables, similarly to the delay free LWR model in Section 4. The delayed LWR model expressed with Lagrangian speed $v(n,t)$ and density $r(n,t)$ can also be found in Burger et al. (2018) and it reads

$$\begin{aligned} \partial_t \frac{1}{r(n,t)} - \partial_n v(n,t) &= 0\,,\\ v(n,t) &= \mathcal{V}(r(n,t-\tau))\,, \end{aligned} \tag{26}$$

cf. (18). Notice that the velocity depends on the past value of the density at time $t-\tau$ instead of the instantaneous value at time t. This model can be transformed to Eulerian framework the same way as (18) in Section 4. The Eulerian model with speed $v(x,t)$ and density $\rho(x,t)$ becomes

$$\begin{aligned} \partial_t \rho(x,t) + \partial_x(\rho(x,t)v(x,t)) &= 0\,,\\ v(x,t) &= \mathcal{V}(\rho(x-\xi,t-\tau))\,, \end{aligned} \tag{27}$$

cf. (19), or with the cumulative flow $N(x,t)$ it reads

$$\partial_t N(x,t) = -\partial_x N(x,t)\mathcal{V}(-\partial_x N(x-\xi,t-\tau))\,, \tag{28}$$

cf. (22).

Notice that the time delay τ is accompanied by a spatial delay ξ in the Eulerian models (27) and (28). This delay originates from the fact that the past time $t-\tau$ corresponds to a past location $x-\xi$ on the highway. The spatial delay ξ is the displacement of vehicle n over $[t-\tau, t]$, which expressed as

$$\xi = X(n,t) - X(n,t-\tau)\,, \tag{29}$$

or

$$\xi = \int_{t-\tau}^{t} v(n,\tilde{t})\mathrm{d}\tilde{t}\,, \tag{30}$$

using Lagrangian traffic measures. The expression of the spatial delay ξ is more complicated in the Eulerian framework. Since time t and position x correspond to the same vehicle as $t-\tau$ and $x-\xi$, the equation defining ξ becomes

$$N(x,t) = N(x-\xi,t-\tau)\,, \tag{31}$$

or, by subtracting $N(x,t-\tau)$ from both sides and using (8) and (4), we can also write

$$\int_{t-\tau}^{t} \rho(x,\tilde{t})v(x,\tilde{t})\mathrm{d}\tilde{t} = \int_{x-\xi}^{x} \rho(\tilde{x},t-\tau)\mathrm{d}\tilde{x}\,. \tag{32}$$

Eqs. (31) or (32) implicitly define the spatial delay ξ as a function of the time delay τ and the states $N(x,t)$ or $\rho(x,t)$ and $v(x,t)$. Both Eulerian formulations, (28) with (31) and (27) with (32), use a PDDE with constant time delay and state-dependent spatial delay. This spatial delay was neglected in the PDDE models constructed in Ngoduy (2014) and Burger et al. (2018). Since state-dependent delays make the analysis of differential equations significantly more difficult (Hartung and Turi, 2000), it is more favorable to use the Lagrangian framework when introducing delays. Lagrangian time delays can naturally be added to the model without modifying argument n. This highlights that in fact the classical Eulerian form (19) of the LWR model is the least suitable form for including (Lagrangian) time delays. In Eulerian framework one needs to consider that past events at time $t-\tau$ took place at location $x-\xi$ (not simply x) due to the propagation of traffic waves.

5.3. Higher order models with delay

The delayed LWR model is the lowest order ($M_X = 1,\ M_v = 0$) special case of PDDE (24). As shown by Appendix, this model exhibits string unstable behavior regardless the value of the delay. However, the main purpose of introducing the delay is tuning string stability properties with the incorporation of a single additional parameter only. In typical car following models, one shall expect string stable behavior for small enough delays and string instability for large delays (Orosz et al., 2010). This cannot be captured by the delayed LWR model; see the proof in Appendix.

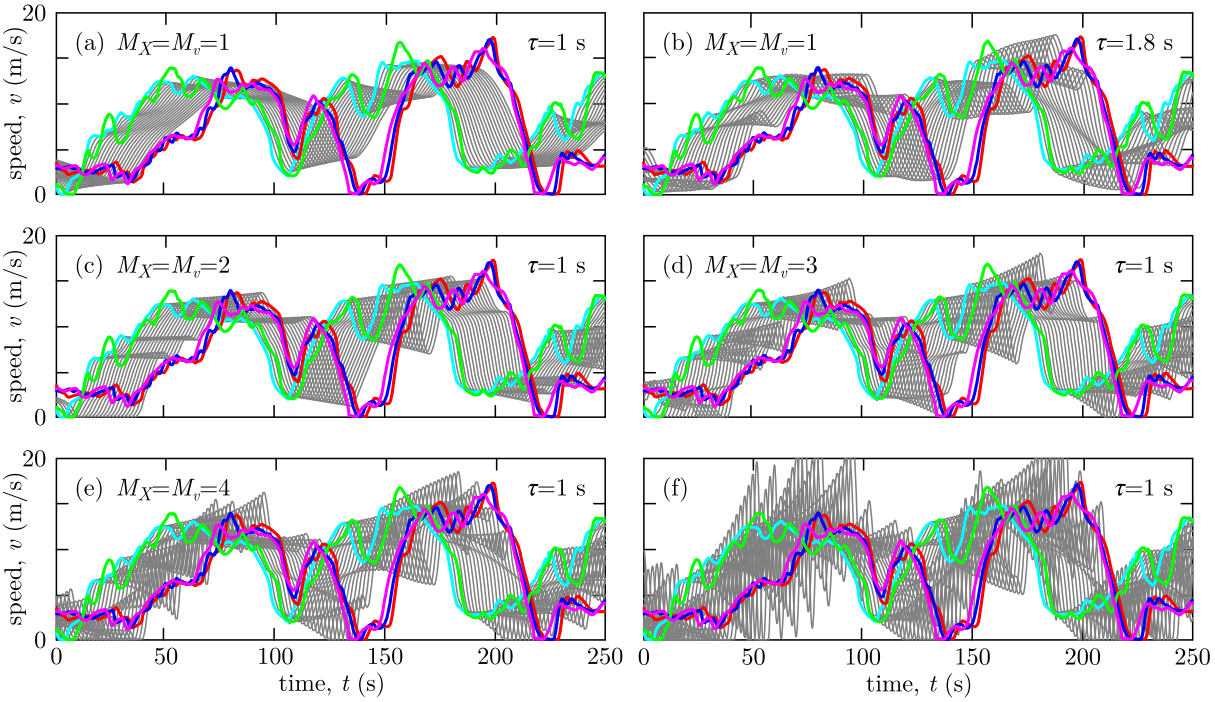

Fig. 9. (a-e) The results of numerical simulations (thin) using the delayed Lagrangian continuum model (24) that was driven by experimental Lagrangian traffic data (thick). The panels correspond to different model orders M_X, M_v and different delays τ as indicated. (f) Simulation results for the discrete car following model (23). The parameters of the models are $d_{\text{st}} = 10\,\text{m}$, $v_{\max} = 30\,\text{m/s}$ and $1/\kappa = 1.5\,\text{s}$. (For interpretation of the references to color in this figure legend, the reader is referred to the web version of this article.)

Therefore, higher order terms in (24) are considered to provide higher fidelity string stability properties. The simplest PDDE with a higher order term is obtained by choosing $M_X = M_v = 1$ in (24):

$$\partial_t X(n,t) - \partial_{tn} X(n,t) = V\left(\partial_n X(n,t-\tau)\right). \tag{33}$$

The performance of this model is evaluated by simulations; see Figs. 9(a,b). All simulations are conducted using a forward-time backward-space finite difference scheme with step sizes $\Delta t = 0.01\,\text{s}$ and $\Delta n = 0.1$. This numerical scheme was chosen because congestion waves propagate forward in time and backward in space (upstream). This scheme was also shown to be the Lagrangian counterpart of the Godunov scheme in Leclercq and Laval (2009) (in the case of the delay free LWR model with piecewise linear fundamental diagram), which is a widely used scheme for kinematic traffic flow models. The boundary condition is still the given measured leader trajectory $X(0,t) = X_0(t)$, whereas the initial condition is $X(n,\theta) = X(0,0) + nd_0$, $\theta \in [-\tau, 0]$, $d_0 = d_{\text{st}}$, since the vehicles started from standstill in the experiment. The parameters κ, d_{st} and $v_{\max}$ are kept the same as in Fig. 8. The delay in Fig. 9(a) is $\tau = 1\,\text{s}$, which is a typical delay considering vehicle dynamics and human driver reaction time (Avedisov et al., 2018). The effect of a larger delay, $\tau = 1.8\,\text{s}$, is shown in Fig. 9(b). This figure proves that by incorporating a single additional parameter, the time delay τ, string (in)stability can be captured, as opposed to the outcome of the LWR model in Fig. 8. The value of the delay even allows us to tune how string (un)stable the results are: small enough delays result in string stable behavior (see Fig. 9(a)), while large delays make the model string unstable (see Fig. 9(b)). This relationship is proven in Appendix, where analytical formulas are derived for the stability limit in terms of the parameters τ and κ.

Stability is also affected by the order of expansion in (24). Fig. 9(c,d,e) present simulation results for second, third and fourth order ($M_X = M_v = 2, 3, 4$) expansions in (24) for $\tau = 1\,\text{s}$. For these higher order models, additional boundary conditions must be defined. For cases $\max(M_X, M_v) \geq 2$, the second boundary condition prescribes $\partial_n X(0,t) = 1/r_0(t)$, which is the inverse of the density perceived by the measured lead vehicle. We approximated this inverse density by applying the inverse of the range policy (12) to the leader's measured speed: $\partial_n X(0,t) \approx V^{-1}(v_0(t))$ (where we prescribed ρ_{st} and ρ_{go} for the non-invertible cases $v_0(t) = 0$ and $v_0(t) \geq v_{\max}$, respectively). For cases $\max(M_X, M_v) \geq 3$, the remaining boundary conditions are $\partial_n^m X(0,t) = 0$, $m = 2, \ldots, \max(M_X, M_v) - 1$, which assume that the local change of density at the leader's position is negligible.

As the orders M_X, M_v are increased, the model behaves in a more string unstable manner, and the stability properties of (24) converge to those of the discrete model (23); see Appendix for proof. Fig. 9(f) shows simulation results for the discrete car following model (23). It can be seen that although the string instability of traffic is captured by low order continuum models, there is difference from the car following model in the degree of instability. The second and third order expansions in Fig. 9(c,d) give reasonably good agreement with the experimental results. This way, PDDE (24) is able to capture (i) the propagation of congestions in time, (ii) the

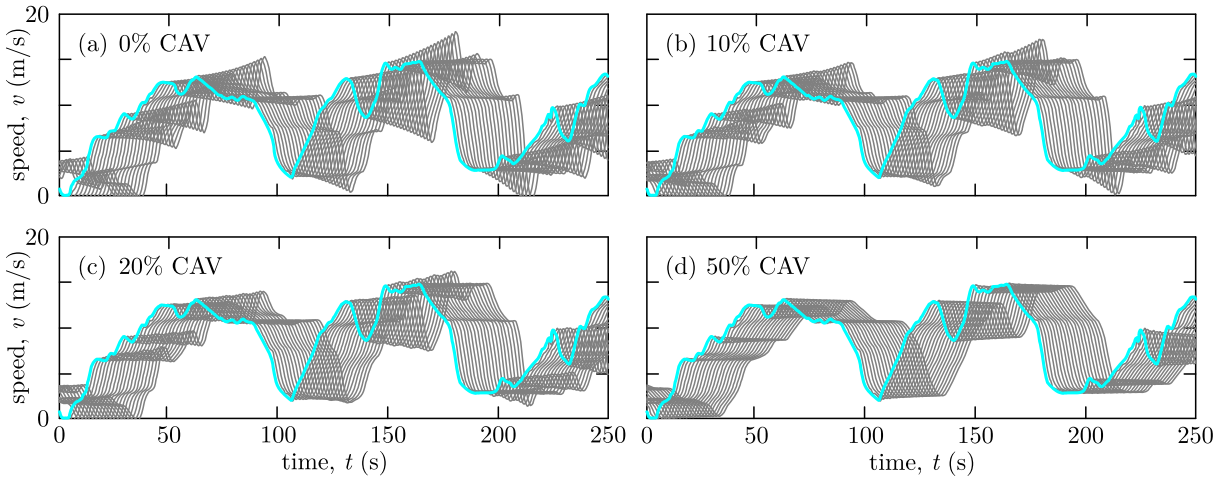

Fig. 10. The results of numerical simulations (thin) using the delayed Lagrangian continuum model (34) that was driven by experimental Lagrangian traffic data (thick cyan). The figure shows the dynamics of heterogeneous traffic flow consisting of connected human-driven vehicles (CHVs) and connected automated vehicles (CAVs). The penetration of CAVs in the traffic flow is indicated in each panel. The order of the model is $M_X = M_v = 3$, the range policy parameters for both CHVs and CAVs are $d_{\mathrm{st}} = 10\,\mathrm{m}$, $v_{\max} = 30\,\mathrm{m/s}$ and $1/\kappa = 1.5\,\mathrm{s}$, whereas the delays associated with CHVs and CAVs are $\tau_{\mathrm{CHV}} = 1\,\mathrm{s}$ and $\tau_{\mathrm{CAV}} = 0.5\,\mathrm{s}$, respectively. (For interpretation of the references to color in this figure legend, the reader is referred to the web version of this article.)

propagation of congestions in space, and (iii) the string (in)stability of traffic, by tuning three parameters: κ, d_{st} and τ. Note that including more higher order terms does not modify the results significantly (qualitatively), but it increases the complexity of the model. Therefore, we refrain from using models of order $M_X > 3$ or $M_v > 3$.

5.4. Extension to heterogeneous traffic flows

Lagrangian models are also well suited for investigating heterogeneous traffic flows. In the near term, there will exist a period of mixed traffic, which involves connected and non-connected, human-driven and automated vehicles as well. For example, CAVs may drive according to a different range policy than the one describing humans, and delays associated with CAVs are typically smaller than the ones related to CHVs. Therefore, the delayed Lagrangian continuum model (24) can be extended to heterogeneous traffic by considering that the range policy and the delay explicitly depend on the vehicle index n, according to the functions $V(n,d)$ and $\tau(n)$, respectively. This leads to

$$\sum_{m=0}^{M_v} \frac{(-1)^m}{m!} \partial_n^m \partial_t X(n,t) = V\left(n, -\sum_{m=1}^{M_X} \frac{(-1)^m}{m!} \partial_n^m X(n, t-\tau(n))\right). \tag{34}$$

Note that explicit time dependency can be considered in a similar manner by taking $V(n,t,d)$ and $\tau(n,t)$.

Model (34) allows one to study the effect of range policy design and delays associated with CAVs on the traffic flow, and also the impact of CAV penetration rate. This is demonstrated in Fig. 10 where mixed traffic is considered with CHVs and 0%, 10%, 20% and 50% penetration of CAVs for the third order case $M_X = M_v = 3$. Here the trajectory of the lead vehicle (thick line) is still taken from the experimental data recorded on a CHV, while the CAVs were injected into the traffic flow in the simulations only, they were not present in the experiment. For simplicity, the range policy $V(n,d)$ is kept the same for all vehicles (independent of n), given by (12) with $d_{\mathrm{st}} = 10\,\mathrm{m}$, $v_{\max} = 30\,\mathrm{m/s}$ and $1/\kappa = 1.5\,\mathrm{s}$ as before. The delay $\tau(n)$, on the other hand, is chosen to be periodic in n with period according to the penetration rate of CAVs. Provided that every Kth vehicle is a CAV, the delay is given by

$$\tau(n) = \begin{cases} \tau_{\mathrm{CAV}} & \text{if } n \in [jK-1, jK), \quad j \in \mathbb{Z}^+, \\ \tau_{\mathrm{CHV}} & \text{otherwise}, \end{cases} \tag{35}$$

where τ_{CAV} and τ_{CHV} are the delays associated with CAVs and CHVs, respectively. Their values are $\tau_{\mathrm{CAV}} = 0.5\,\mathrm{s}$ and $\tau_{\mathrm{CHV}} = 1\,\mathrm{s}$ in Fig. 10. Note that any arbitrary delay function $\tau(n)$ could be considered similarly, and the range policy parameters d_{st}, d_{go} and $v_{\max}$ could also be vehicle-dependent analogously.

Fig. 10 shows that as the penetration of CAVs is increased, they are able to mitigate traffic congestions with smooth driving. Although a relatively large penetration is required in this simple example to achieve this goal, other, more sophisticated control laws leveraging connectivity with multiple vehicles could also be applied to provide benefits even at low penetrations; see Ge et al. (2018), Cui et al. (2017), Stern et al. (2018), Wu et al. (2017) and Zheng et al. (2020). The control of CAVs is out of scope of this paper, but here we highlight that Lagrangian approaches are suited for control design and penetration studies. We remark that one can also utilize multi-class traffic models (van Wageningen-Kessels et al., 2010; Leclercq and Laval, 2009; Piacentini et al., 2019) to study heterogeneous traffic flows, or coupled Eulerian–Lagrangian approaches (Čičić and Johansson, 2018; Jin et al., 2018) which allow large-scale penetration studies while incorporating Eulerian data as well.

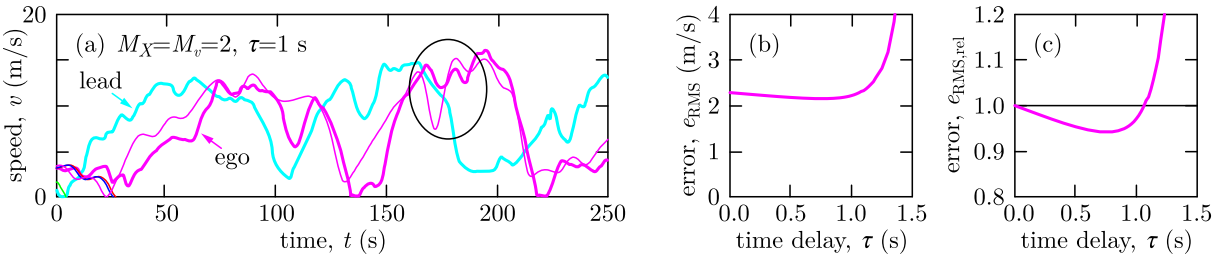

Fig. 11. (a) Speed estimation for an ego vehicle (thin magenta) obtained from the delayed Lagrangian continuum model (24) based on the trajectory data (thick cyan) communicated through V2X connectivity. The actual measured speed signal of the ego vehicle is also shown (thick magenta). The parameters of the model are $M_X = M_v = 2$, $d_{\mathrm{st}} = 10\,\mathrm{m}$, $v_{\max} = 30\,\mathrm{m/s}$, $1/\kappa = 1.5\,\mathrm{s}$ and $\tau = 1\,\mathrm{s}$. (b) The RMS error of the speed estimation as a function of the delay parameter τ. (c) The RMS error relative to the delay free case $\tau = 0$. (For interpretation of the references to color in this figure legend, the reader is referred to the web version of this article.)

6. Traffic prediction based on V2X connectivity

The delayed Lagrangian continuum model (24) can be utilized by connected vehicles to make traffic predictions based on available V2X communication data. If a CV receives trajectory data from another CV downstream, it can use the data as boundary condition to simulate model (24) forward in time. The simulated trajectories represent an estimation of the traffic flow, and they can be used to predict the future motion of the upstream CV or its predecessors. Such on-board predictions can be tailored to the needs of the CV, whom may exploit them to plan and control its motion or to optimize its operation. Below we demonstrate such prediction capability by considering that trajectory data from a downstream lead vehicle (thick cyan in Fig. 9) is transmitted to an ego vehicle (thick magenta in Fig. 9) via V2X connectivity. First we calculate the potentially achievable accuracy of model (24) by comparing simulations to measured trajectories offline. Then we discuss how predictions about the future can be made in real time, on board of the ego CV.

6.1. Model-based traffic estimation and its accuracy

In order to quantify the accuracy of model (24), we simulated it by utilizing the lead vehicle's measured trajectory (thick cyan) as boundary condition; see Fig. 9. Then we compared the results to the measured trajectory of a given ego vehicle (thick magenta). Note that in practice it is unknown how many vehicles are located between the lead and the ego vehicle, i.e., the vehicle index n is not known for the communicated trajectory data. Still, the number of vehicles between the lead and the ego vehicle can be estimated based on their positions. Therefore, at each time instant t we selected a simulated vehicle $n_{\mathrm{e}}(t)$ whose position $X(n_{\mathrm{e}}(t), t)$ is closest to the measured ego vehicle. The speed $v(n_{\mathrm{e}}(t), t)$ of the selected simulated vehicle can be considered as a model-based estimation of the speed of the ego vehicle. This estimation is depicted by a thin magenta line in Fig. 11(a), whereas the actual measured motion is indicated by a thick magenta line. The parameters here are the same as in Fig. 9(c).

By comparing the model outcome (thin magenta) to the ground truth (thick magenta) we can confirm that the general trend of speed fluctuations is well captured by the model. With the selected delay $\tau = 1\,\mathrm{s}$, the model exhibits string unstable behavior, which was indeed observed during the majority of the experiment. However, an apparent qualitative mismatch occurs between the prediction and experiment in the region marked by circle. Here the experimental vehicles started to attenuate velocity fluctuations instead of behaving in a string unstable manner. Model (24) with a fixed delay τ is not able to capture such changes in driving behavior over time, but it could potentially be captured by time varying parameters (such as delay $\tau(t)$) or more detailed models (such as acceleration-based ones).

We quantified the error of the model-based speed estimation for various values of the constant delay τ. We calculated the root mean square (RMS) error e_{RMS} between the calculated and measured speed for the ego vehicle over the time interval shown in Fig. 11(a) as a function of the delay τ; see Fig. 11(b). Fig. 11(c) shows the relative error $e_{\mathrm{RMS,rel}}(\tau) = e_{\mathrm{RMS}}(\tau)/e_{\mathrm{RMS}}(0)$ with respect to the delay free case $\tau = 0$. It can observed that there is an optimal, nonzero value of the delay that gives the most accurate speed estimation based on this metric (which is $\tau \approx 0.8\,\mathrm{s}$ in this example). Figs. 9 and 11 highlight that the delay parameter τ should be selected carefully: too small delay results in string stable behavior instead of the typical string unstable one (i.e., qualitative mismatch), whereas too large delay results in excessive string instability and large error (i.e., quantitative mismatch). We remark that here the speed signals were used directly, while various average speed measures also exist to evaluate the performance of traffic flow models (Jamshidnejad and De Schutter, 2015).

6.2. Towards on-board traffic prediction

One significant benefit of the delayed Lagrangian continuum model (24) is that it allows one to predict the future state of traffic on board in an online fashion. To make a prediction at time t_{p}, trajectory data over $t \le t_{\mathrm{p}}$ can be utilized only, while no data are available over $t > t_{\mathrm{p}}$. This is illustrated in Fig. 12(a) for $t_{\mathrm{p}} = 120\,\mathrm{s}$, where the trajectories available for prediction are shown by thick

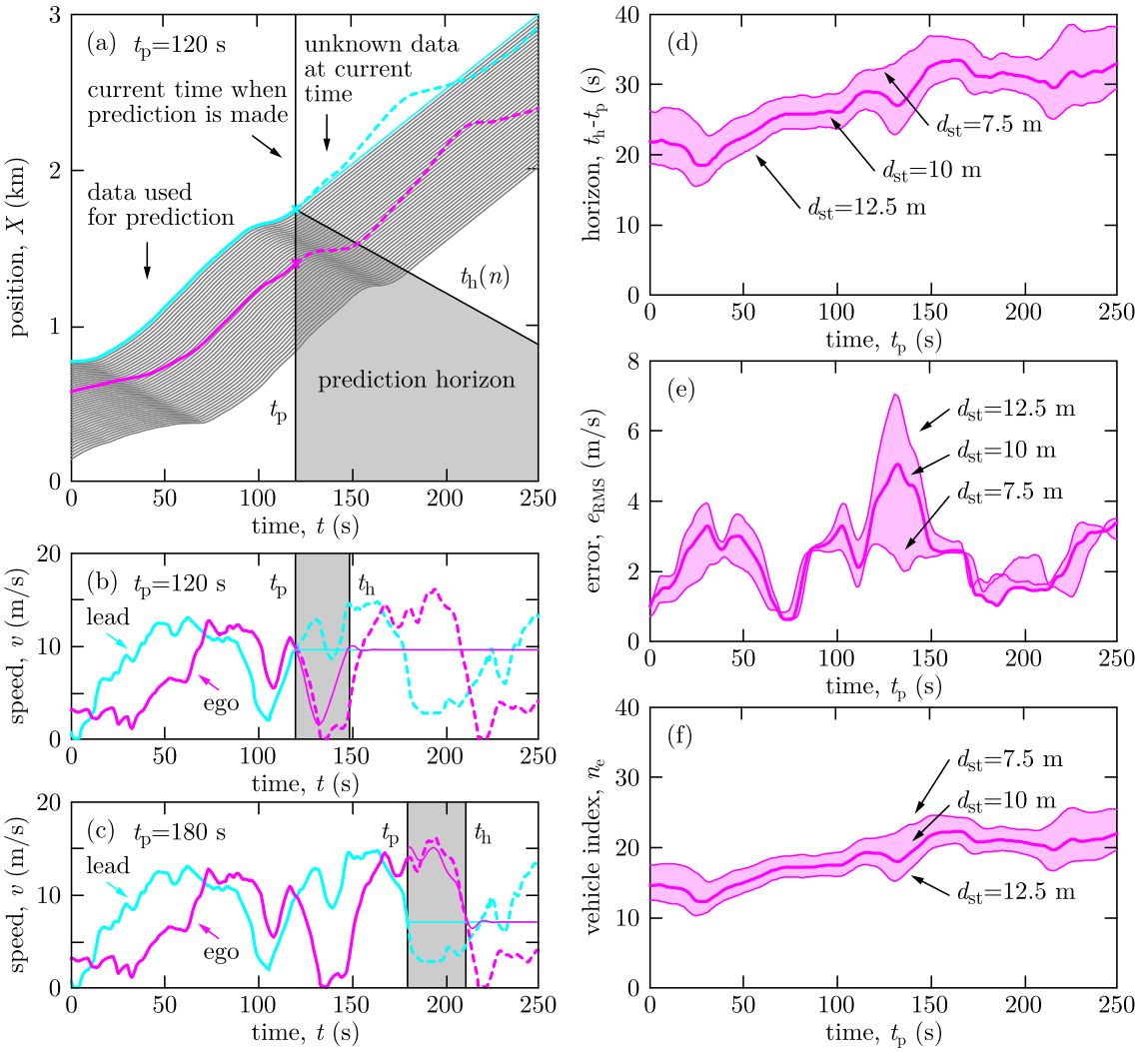

Fig. 12. Illustration of connectivity-based on-board traffic prediction via the delayed Lagrangian continuum model (24). The measured trajectories that are available for prediction via V2X connectivity are shown by thick solid lines, whereas the measured trajectories that are not yet available at the time of prediction are indicated by dashed lines. (a) Simulated trajectories (thin lines) representing the predicted position after $t_p = 120$ s. (b,c) Speed predictions (thin lines) corresponding to the experimentally measured connected vehicles after $t_p = 120$ s and $t_p = 180$ s, respectively. The relevant prediction horizon is shaded with gray. (d) The prediction horizon, (e) the RMS prediction error and (f) the estimated vehicle index as a function of time. The model parameters are $M_X = M_v = 2$, $d_{st} = 10$ m, $v_{max} = 30$ m/s, $1/\kappa = 1.5$ s and $\tau = 1$ s. (For interpretation of the references to color in this figure legend, the reader is referred to the web version of this article.)

solid lines, whereas the unavailable data (measured after t_p) is depicted by dashed lines. The aim is to predict an ego vehicle's future motion (dashed magenta) based on a lead vehicle's motion measured up to t_p (thick cyan).

Fig. 12(a) illustrates simulation results (thin lines) based on the lead vehicle's measured trajectory (thick cyan) for the same parameters as in Fig. 9(c). The predicted trajectory of a given ego vehicle (magenta) can be obtained from the simulation results similarly to Section 6.1. At time t_p we select the simulated vehicle $n_e(t_p)$ whose position $X(n_e(t_p), t_p)$ is closest to the measured ego vehicle. Then the speed $v(n_e(t_p), t)$ of the simulated vehicle is the predicted speed of the ego vehicle over $t > t_p$. Fig. 12(b,c) illustrate the speed prediction (thin magenta) for $t_p = 120$ s and $t_p = 180$ s, respectively. The prediction (thin magenta) closely matches measured results (dashed magenta).

Note that in order to simulate model (24) into the future, the lead vehicle's trajectory must also be predicted for $t > t_p$. Here we use the constant speed prediction $X(0,t) \approx X(0,t_p) + v(0,t_p)(t - t_p)$ for $t > t_p$; see the thin cyan lines in Figs. 12(a-c). Although the lead vehicle's predicted speed (thin cyan) does not match its actual future speed (dashed cyan), the simulated trajectories are still valid over a horizon $t \in [t_p, t_h(n)]$, since the lead vehicle's speed fluctuations up to present (thick cyan) propagate and affect the upstream traffic in the future. Fig. 12(a) shows that the farther the simulated vehicles are from the lead vehicle at t_p, the larger the horizon $t_h(n)$ (it monotonically increases with decreasing n). Beyond the horizon the predicted speeds tend to a constant due to the constant speed prediction about the lead vehicle. Thus, predictions are valid only until the horizon is reached.

The prediction horizon for the ego vehicle (measured by $t_h(n_e) - t_p$) is plotted in Fig. 12(d). The prediction horizon $t_h(n)$ can be calculated as follows for the simplest special case of the model. Recall that when the middle, linear part of the range policy (12) is effective for the LWR model ($M_X = 1$, $M_v = 0$, $\tau = 0$), the solutions are the traveling waves given by (15). Substituting $t = t_h(n)$ and $t + n/\kappa = t_p$ into (15) gives the prediction horizon for vehicle n implicitly by

$$X(n, t_h(n)) = X(0, t_p) - w(t_h(n) - t_p), \tag{36}$$

where $w = \kappa d_{st}$ denotes the wave speed. Formula (36) was evaluated numerically to generate Fig. 12(d). The implicit formula can be reduced to the explicit expression

$$t_h(n) = t_p + \frac{X(0, t_p) - X(n, t_p)}{v(n, t_p) + w} \tag{37}$$

if the speed of vehicle n is constant $v(n,t) \equiv v(n, t_p)$ over $t \in [t_p, t_h(n)]$. Formula (37) gives an estimate for the general case of model (24) and for non-constant speed as well, and it shows approximately how far the ego vehicle needs trajectory data from to achieve a desired prediction horizon.

Fig. 12(e) shows the RMS error of the ego vehicle's speed prediction relative to its measured speed as a function of time. The error was calculated over the prediction horizon shown by the gray shading in Fig. 12(b,c) and by the curve in Fig. 12(d). The RMS error in Fig. 12(e) is typically around 2 m/s, and an example for larger prediction error is illustrated in Fig. 12(b) where the larger error is mainly caused by the time mismatch between the predicted and the actual speed fluctuations.

Finally, Fig. 12(f) indicates the estimated vehicle index n_e of the ego vehicle. Note that the vehicle index is unknown in practice and its estimate is an outcome of the prediction algorithm. To investigate sensitivity with respect to vehicle index estimation, we ran simulations with three different parameters, $d_{st} = 7.5$, 10 and 12.5 m, and evaluated n_e along with the prediction horizon and accuracy; see Figs. 12(d-f). The three different parameter values cover a relatively large range of wave speeds: $w = 5$, 6.7 and 8.3 m/s. According to Fig. 12(f), significant changes in the wave speed affect the estimated vehicle index, prediction horizon and accuracy, but the results are acceptable if the wave speed is kept reasonably low.

The method described above allows V2X connectivity-based traffic prediction on board of CVs. To have large enough prediction horizon, V2X connectivity must provide trajectory information from far enough distance downstream the ego vehicle. Note that the range of vehicle-to-vehicle (V2V) connectivity is limited, thus to extend this range and achieve a large prediction horizon, one shall utilize other means of V2X connectivity as well, such as vehicle-to-infrastructure (V2I) communication. In addition, the trajectory information must be available over a sufficient duration of time: approximately the same duration as the desired prediction. Finally, to have large enough update rate of prediction (i.e., to be able to update t_p frequently), the simulations must be done in a computationally efficient manner. However, going into details about computational efficiency for real-time applications is out of scope of this paper.

7. Conclusions and future work

This paper presented an approach to build Lagrangian continuum models that directly exploit the availability of vehicle trajectory data provided by vehicle-to-everything (V2X) connectivity. The constructed model, given by (24), was able to capture three essential phenomena: the propagation of congestions in time, the propagation of congestions in space, and the string (in)stability of traffic, by involving only three tunable parameters. One of these parameters was the time delay that was included to model the vehicle dynamics, driver reaction time, feedback delays and communication delays. The incorporation of delays into continuum models is nontrivial, this is one of the key theoretical contributions of this work. It was shown that the Lagrangian framework is more convenient to do this, and that the order of the model must be selected carefully to capture string stability properties. The performance of the model was demonstrated by simulations, and string stability conditions were derived analytically to analyze the effect of delays on the traffic flow.

The constructed model can be directly utilized by connected vehicles (CVs) to make Lagrangian traffic predictions. Via V2X connectivity, a CV may obtain information about the motion of other connected vehicles ahead and may use these data to simulate model (24) to predict downstream traffic. Via the prediction, the CV is able to estimate the motion of preceding non-connected vehicles, as well as its own anticipated future behavior in traffic (for instance, when and where it is expected to meet a congestion and how much it shall decelerate). Provided that predictions are made on board, this information can be utilized in the control design of connected automated vehicles (CAVs) to optimize their operation, or to make anticipative actions and facilitate smooth driving, which is beneficial for both the CAV and the surrounding traffic. These benefits include mitigating traffic congestions, reducing the energy consumption of CAVs and other neighboring vehicles, as well as facilitating the optimal operation of on-board systems relying on speed previews. In this paper, we focused on predicting traffic in the scale of minutes involving dozens of vehicles, while looking at traffic at larger scale is left future research.

The predictions show the usefulness of Lagrangian models. In Lagrangian framework, trajectory data can directly be utilized as boundary condition, delays can naturally be taken into account, and the resulting predictions can be tailored to the needs of CVs. In addition, it is natural to extend Lagrangian models to consider heterogeneous traffic flows with a mixture of human-driven and connected automated vehicles. This allows one to study how the penetration of CAVs and their control design affect the overall traffic flow. A potential future extension of this work is investigating multi-lane and multi-class traffic to further characterize the effect of CAVs on the flow.

Note that the results of Lagrangian models can be converted to Eulerian traffic measures. This facilitates the fusion of models in the two frameworks and the creation of coupled models. Future work may focus on integrating Lagrangian and Eulerian approaches to be able to consider vehicle-based information (trajectory data) and location-based information (related to road, infrastructure and geography) at the same time.

Finally, although this paper is restricted to velocity-based, so-called kinematic models, the approach of constructing and using delayed Lagrangian continuum models can be applied at the acceleration level, too. Our future work includes the extension of this concept to acceleration-based models. One important feature of these models is that they directly take into account the acceleration capabilities (limits) of vehicles. Furthermore, since these models involve the commanded acceleration, they are more suitable for control design of CAVs.

CRediT authorship contribution statement

Tamás G. Molnár: Responsible for the modeling, analysis and simulations, contributed with ideas and discussions to this research, writing the paper. **Devesh Upadhyay:** Participated in the experiments, contributed with ideas and discussions to this research, writing the paper. **Michael Hopka:** Participated in the experiments, contributed with ideas and discussions to this research, writing the paper. **Michiel Van Nieuwstadt:** Participated in the experiments, contributed with ideas and discussions to this research, writing the paper. **Gábor Orosz:** Responsible for the modeling, analysis and simulations, contributed with ideas and discussions to this research, writing the paper. All authors gave final approval for publication.

Acknowledgments

The authors would like to thank Cory Hendrickson, Chaozhe He and Sergei Avedisov for the useful discussions on this topic and for their valuable ideas and feedback. This project was funded by Ford Motor Co., United States also received funding from the Rosztoczy Foundation, United States. The supports are really appreciated.

Appendix. String stability analysis

Here, we prove that the constructed models are well-posed in terms of stability properties. We analyze the string stability of the continuum model (24) and make comparison with the discrete model (23) based on our previous work in Molnár et al. (2019). Physically, string stability means the attenuation (decay) of velocity fluctuations along a chain of vehicles, which is directly related to the mitigation of congestion waves on highways. That is, string stability is essentially the stability of solutions with respect to the vehicle index n. Note, however, that string stability has various different mathematical definitions, see Feng et al. (2019) for a summary about this topic. Here we consider linear input-to-output string stability with respect to $\mathcal{L}_2$ norm and we aim to find the string stable domains in the space of the parameters τ and κ.

We restrict our discussion to linear stability and smooth solutions; shock solutions (Daganzo, 1994) (caused by Eulerian boundary conditions) are out of scope of this work. Note that shock-like physical behavior on highways can still be captured by the Lagrangian models, since they are able to reproduce large decelerations and accelerations for the vehicles (whose trajectory is a smooth function), and they are also able to exhibit stop-and-go motion (Orosz et al., 2010). For more details on well-posedness and smoothness of solutions, the reader is referred to Daganzo (2006) and van Wageningen-Kessels et al. (2013). In what follows, we prove that the stability boundaries of (24) converge to those of (23) as the orders M_X, M_v are increased, and we show that properly selected low order models already have realistic string stability properties.

A.1. String stability condition

In what follows, we analyze the string stability of the uniform flow $v(n,t) \equiv v^*$ of constant speed v^*. We consider perturbations $\tilde{v}(n,t)$ around the uniform flow in the form $v(n,t) = v^* + \tilde{v}(n,t)$ and we linearize the governing equations. If the system is string stable, these perturbations decay upstream along a string of vehicles as n is decreased.

In particular, we assume harmonic velocity perturbations of angular frequency $\omega > 0$ in the form

$$\tilde{v}(n,t) = v_{\text{amp}} \mathrm{e}^{\mathrm{i}\omega t} \mathrm{e}^{-\lambda(\omega) n}\,, \tag{A.1}$$

where an exponential trial solution is assumed in terms of variable n for the linearized system. Note that general velocity fluctuations can be decomposed into such harmonics. In (A.1) $\lambda(\omega)$ determines how velocity fluctuations of a given angular frequency ω propagate along a string of vehicles. The real part of $\lambda(\omega)$ determines whether the fluctuations amplify or decay: $\Re(\lambda(\omega)) < 0$ must hold for all $\omega > 0$ to guarantee the decay of velocity fluctuations upstream (as $n \to -\infty$). The imaginary part $k = \Im(\lambda(\omega))$ is the wave number, which defines the angular frequency of fluctuations with respect to the vehicle index n. Note that the sign of k also indicates the direction of wave propagation: waves with $k < 0$ ($k > 0$) propagate upstream (downstream).

During string stability analysis we disregard wave numbers below $-\pi$ and above π for the following reason. When traffic models are evaluated physically, solutions are considered at integer vehicle indices only, which implies a sampling with period 1 in terms of the variable n. According to the Nyquist–Shannon sampling theorem, phenomena of period smaller than 2 (wave number larger than π) cannot be captured by sampling with period 1. Thus, we formulate the condition for string stability as

$$\Re(\lambda(\omega)) < 0\,, \quad \forall \omega > 0 \tag{A.2}$$

subject to $\Im(\lambda(\omega)) \in [-\pi, \pi]$.

For discrete models, the exclusion of wave numbers outside $[-\pi, \pi]$ naturally happens. In such models, the expression $T(\mathrm{i}\omega) = \exp(\lambda(\omega))$ appears instead of $\lambda(\omega)$, which is in fact the transfer function between the lead vehicle's velocity fluctuations $\tilde{v}(n+1,t)$ and the follower vehicle's velocity fluctuations $\tilde{v}(n,t)$ (Zhang and Orosz, 2016). Accordingly, the string stability condition (A.2) can be re-written as

$$|T(\mathrm{i}\omega)| = \left|\mathrm{e}^{\lambda(\omega)}\right| < 1, \quad \forall \omega > 0\,, \tag{A.3}$$

that is, the vehicle pair as an input–output system shall not amplify velocity fluctuations.

Conditions (A.2) and (A.3) define the string stable domains in the space of the parameters such as τ and κ. If (A.2) and (A.3) are algebraically too complex to evaluate, we may also search for the string stability boundaries rather than the string stable parameter domains. At the stability boundary, velocity fluctuations neither amplify nor decay along a string of vehicles, thus we can use the ansatz

$$\tilde{v}(n,t) = v_{\mathrm{amp}} \mathrm{e}^{\mathrm{i}\omega t} \mathrm{e}^{-\mathrm{i}kn}\,, \tag{A.4}$$

where $k \in [-\pi, \pi]$. Using this trial solution, stability boundaries can be constructed for various values of k and their envelope – which can be depicted, but might be too difficult to calculate explicitly – defines the string stability limit.

In what follows we carry out the string stability analysis first for the discrete model (23), then for the continuum model (24). As a result, we depict stability charts indicating the string stable domains in the (τ, κ) plane.

A.2. String stability analysis of the delayed discrete model

In order to analyze string stability, we linearize (23) around the uniform flow $v(n,t) \equiv v^*$, $X(n,t) = X(0,0) + v^* t + n d^*$ associated with uniform distance d^* that satisfies $V(d^*) = v^*$. To accommodate our linear system to the string stability conditions above, we first differentiate (23) with respect to time before linearization and write the linear system at the velocity level. Assuming the nontrivial case $d_{\mathrm{st}} < d^* < d_{\mathrm{go}}$, we obtain

$$\partial_t \tilde{v}(n,t) = \kappa(\tilde{v}(n+1, t-\tau) - \tilde{v}(n, t-\tau))\,, \tag{A.5}$$

where $\kappa = V'(d^*) > 0$ is the slope of the range policy (12).

Substitution of (A.1) into (A.5) leads to the characteristic equation of the discrete model in the form

$$\mathrm{i}\omega \mathrm{e}^{\mathrm{i}\omega\tau} \mathrm{e}^{\lambda(\omega)} = \kappa\left(1 - \mathrm{e}^{\lambda(\omega)}\right), \tag{A.6}$$

which can be rearranged to

$$T(\mathrm{i}\omega) = \mathrm{e}^{\lambda(\omega)} = \frac{\kappa}{\mathrm{i}\omega \mathrm{e}^{\mathrm{i}\omega\tau} + \kappa}\,. \tag{A.7}$$

Then $\lambda(\omega)$ can be calculated and plotted in the complex plane as a curve parameterized by ω. This spectrum plot is illustrated in the bottom right panel of Fig. A.13(a) for $\tau = 0$ and Fig. A.13(b) for $\tau = 1\,\mathrm{s}$, assuming $\kappa = 0.6\,\mathrm{s}^{-1}$. Recall that the system is string stable if the spectrum is located in the left half plane (see the $\tau = 0$ case), and string unstable otherwise (see the $\tau = 1\,\mathrm{s}$ case). Also note that the range of the vertical axis is $\Im(\lambda(\omega)) \in [-\pi, \pi]$.

Eqs. (A.3) and (A.7) imply the following string stability condition for the discrete model (23):

$$2\kappa\tau \frac{\sin(\omega\tau)}{\omega\tau} - 1 < 0\,, \quad \forall \omega > 0\,. \tag{A.8}$$

For $\tau = 0$, the system is string stable for any κ. For $\tau > 0$, the critical case $\omega \to 0^+$ gives the largest left-hand side in (A.8), which implies the following string stability condition for the discrete model (23):

$$\tau < \tau_{\mathrm{cr}} = \frac{1}{2\kappa}\,. \tag{A.9}$$

The same result can also be obtained via substituting the ansatz (A.4) into the linearized discrete model (A.5). This leads to the characteristic equation

$$\mathrm{i}\omega \mathrm{e}^{\mathrm{i}\omega\tau} = \kappa\left(\mathrm{e}^{-\mathrm{i}k} - 1\right), \tag{A.10}$$

which, after separation into real and imaginary parts, yields

$$\begin{aligned} -\omega \sin(\omega\tau) &= \kappa(\cos k - 1)\,, \\ \omega \cos(\omega\tau) &= -\kappa \sin k\,. \end{aligned} \tag{A.11}$$

By the help of dividing these two equations, we can express the parameters τ and κ as

$$\begin{aligned} \tau &= \frac{1}{\omega}\left(j\pi - \frac{k}{2}\right), \\ \kappa &= \frac{\omega(-1)^{j+1}}{2\sin\left(\frac{k}{2}\right)}\,, \end{aligned} \tag{A.12}$$

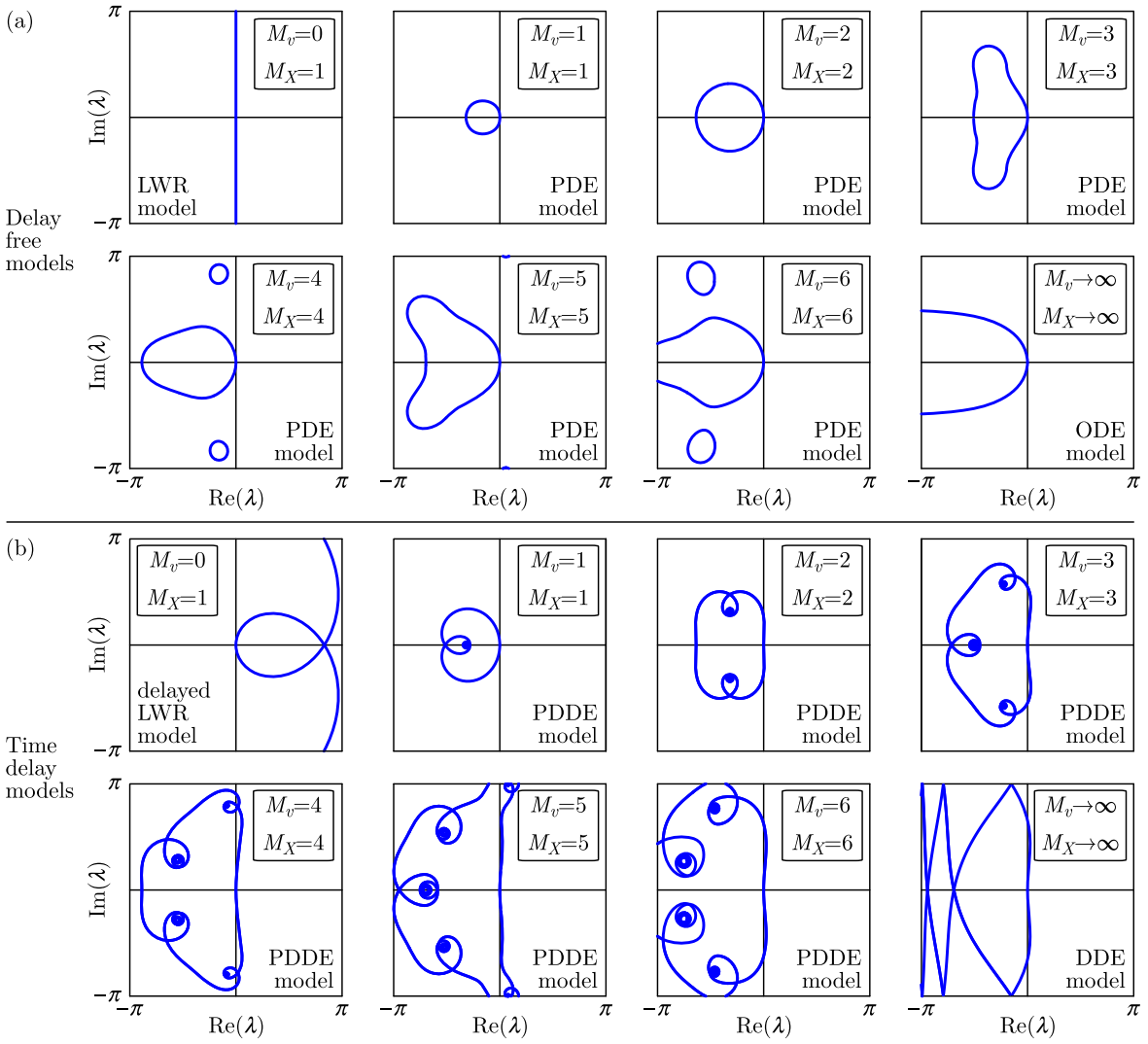

Fig. A.13. (a) The spectrum of delay free models: the LWR model (14), PDE (13) of various orders and ODE (11) assuming $\kappa = 0.6\ \mathrm{s}^{-1}$. (b) The spectrum of time delay models: the delayed LWR model (25), PDDE (24) of various orders and DDE (23) assuming $\kappa = 0.6\ \mathrm{s}^{-1}$, $\tau = 1\ \mathrm{s}$.

$j \in \mathbb{Z}$. For each j, (A.12) defines a family of curves in the (τ, κ) plane where each value of k implies a different curve parameterized by ω. The family of curves for $j = 0$ is illustrated in the top right panel of Fig. A.14. Note that $j = 0$ gives the smallest, critical delay. It can be shown that the envelope of these stability boundaries is exactly the hyperbola given by (A.9), see the dashed line in the figure.

A.3. String stability analysis of the delayed continuum model

The linearized counterpart of the continuum model (24) reads

$$\sum_{m=0}^{M_v} \frac{(-1)^m}{m!} \partial_n^m \partial_t \tilde{v}(n,t) = -\kappa \sum_{m=1}^{M_X} \frac{(-1)^m}{m!} \partial_n^m \tilde{v}(n, t-\tau)\,. \tag{A.13}$$

Substitution of (A.1) into (A.13) yields the characteristic equation of the continuum model in the form

$$\mathrm{i}\omega \mathrm{e}^{\mathrm{i}\omega\tau} \sum_{m=0}^{M_v} \frac{\lambda(\omega)^m}{m!} = -\kappa \sum_{m=1}^{M_X} \frac{\lambda(\omega)^m}{m!}\,. \tag{A.14}$$

Notice that (A.14) involves a polynomial of $\lambda(\omega)$, which can also be obtained from (A.6) via Taylor expansion of the exponential terms.

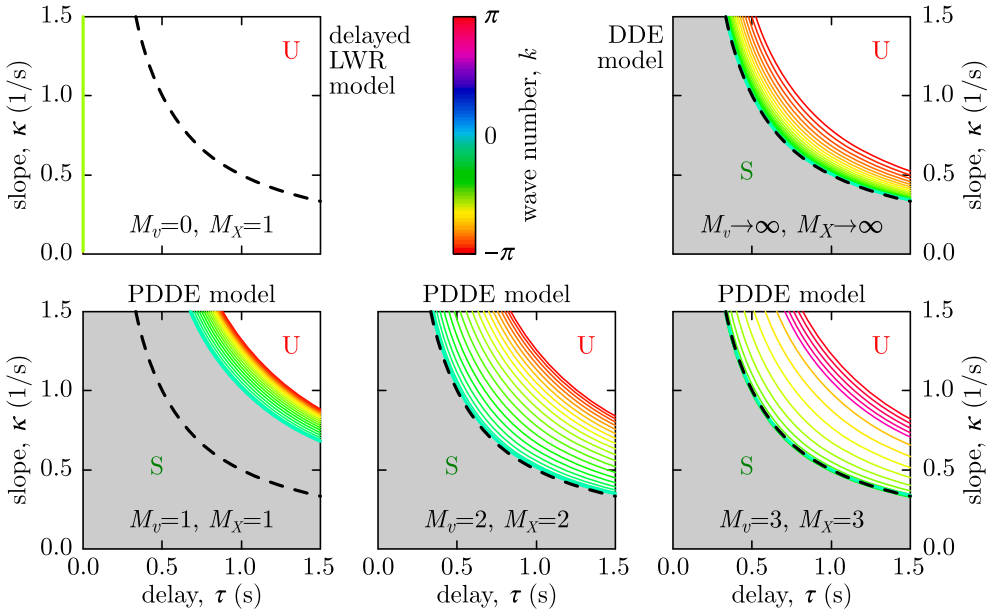

Fig. A.14. Stability charts of time delay models: the delayed LWR model (25), DDE (23) and PDDE (24) of various orders. The string stable region (S) is shaded with gray, while the string unstable region (U) is white. Colorful thin lines show the stability boundaries given by (A.12) and (A.20) for various wave numbers k. Black dashed line indicates the critical delay (A.9) of the discrete model (23) for reference. (For interpretation of the references to color in this figure legend, the reader is referred to the web version of this article.)

String stability can be evaluated based on (A.2) provided that $\lambda(\omega)$ can be expressed from (A.14). This is possible for low order PDDE models (small M_X and M_v). For the delayed LWR model (25) ($M_X = 1$, $M_v = 0$), we obtain

$$\lambda(\omega) = -\frac{\mathrm{i}\omega \mathrm{e}^{\mathrm{i}\omega\tau}}{\kappa}. \tag{A.15}$$

The corresponding spectrum plot is shown by the top left panel of Figs. A.13(a,b) for $\tau = 0$ and $\tau = 1\,\mathrm{s}$, respectively. The figure reveals that the delay free LWR model is at the boundary of string stability, since its spectrum is located on the imaginary axis for any $\kappa > 0$. This explains why string (in)stability cannot be captured by the LWR model. Meanwhile, the delayed LWR model is string unstable for any $\tau > 0$ and $\kappa > 0$, because its spectrum is located in the right half plane for small enough ω (i.e., $\Re(\lambda(\omega)) \to 0^+$ as $\omega \to 0^+$). The instability is also illustrated by the top left panel of Fig. A.14, where a stability boundary $\tau = 0$ (green) shows up in the stability chart. This justifies that the higher order terms in Section 5.3 are required for the PDDE models to achieve realistic string stability properties.

The spectrum of model (33) with first order expansion ($M_X = M_v = 1$) can also be calculated in closed form:

$$\lambda(\omega) = \frac{\mathrm{i}\omega \mathrm{e}^{\mathrm{i}\omega\tau}}{\kappa + \mathrm{i}\omega \mathrm{e}^{\mathrm{i}\omega\tau}}. \tag{A.16}$$

However, analytical results for spectra become too complicated or unavailable for higher M_X and M_v orders. Still, $\lambda(\omega)$ can be calculated numerically for each value of ω and can be plotted in the complex plane. This is shown by the spectrum plots in Fig. A.13(a) for $\tau = 0$ and Fig. A.13(b) for $\tau = 1\,\mathrm{s}$. The different panels of the figure present the spectrum of PDDEs of different order. Note that only the delayed LWR model has a spectrum that bends to the right near the origin and exhibits string instability for any delay. For other, higher order models string stability can also be achieved if the delay is small enough.

Fig. A.13 demonstrates that for both $\tau = 0$ and $\tau > 0$ the spectrum of the PDDE converges near the origin to that of the DDE as the orders M_X and M_v are increased. The behavior of the spectrum close to the imaginary axis (i.e., the stability properties) are well captured even by low order models (for example $M_X = M_v = 3$). Including more terms ($M_X > 3$ or $M_v > 3$) modifies the spectrum near the imaginary axis only for high imaginary parts (wave numbers), which are less significant from practical point of view. Therefore, there is no need to add terms of order above $M_X = M_v = 3$, since they increase the complexity of the model. The selection of order $M_X = M_v = 2$ or $M_X = M_v = 3$ is sufficiently high for capturing string stability properties while keeping the model reasonably simple.

To calculate the string stability boundaries of higher order models, we use the ansatz (A.4) and substitute it into the continuum model (A.13). This gives the characteristic equation

$$\mathrm{i}\omega \mathrm{e}^{\mathrm{i}\omega\tau}(1 + B_v + \mathrm{i}A_v) = -\kappa(B_X + \mathrm{i}A_X), \tag{A.17}$$

where the B_X, B_v and A_X, A_v are the real and imaginary parts of the Taylor expansions of $e^{ik} - 1$ up to order M_X, M_v:

$$B_X = \sum_{l=1}^{\lfloor M_X/2 \rfloor} \frac{(-1)^l k^{2l}}{(2l)!}, \quad A_X = \sum_{l=1}^{\lfloor (M_X+1)/2 \rfloor} \frac{(-1)^{l-1} k^{2l-1}}{(2l-1)!}, \quad B_v = \sum_{l=1}^{\lfloor M_v/2 \rfloor} \frac{(-1)^l k^{2l}}{(2l)!}, \quad A_v = \sum_{l=1}^{\lfloor (M_v+1)/2 \rfloor} \frac{(-1)^{l-1} k^{2l-1}}{(2l-1)!}. \tag{A.18}$$

Separation of (A.17) into real and imaginary parts yields

$$\begin{aligned} -\omega \sin(\omega\tau)(1 + B_v) - \omega \cos(\omega\tau) A_v &= -\kappa B_X, \\ \omega \cos(\omega\tau)(1 + B_v) - \omega \sin(\omega\tau) A_v &= -\kappa A_X. \end{aligned} \tag{A.19}$$

After rearranging these equations, the string stability boundaries become

$$\begin{aligned} \tau &= \frac{1}{\omega} \left(\arctan\left(\frac{A_v A_X + B_v B_X + B_X}{A_v B_X - B_v A_X - A_X} \right) + j\pi \right), \\ \kappa &= \frac{1}{A_X} \left(\omega \sin(\omega\tau) A_v - \omega \cos(\omega\tau)(1 + B_v) \right), \end{aligned} \tag{A.20}$$

$j \in \mathbb{Z}$.

Eq. (A.20) defines a family of curves in the (τ, κ) plane, which is shown in Fig. A.14 for $M_X = M_v = 1, 2, 3$ and $j = 0$. The envelope of these curves defines the string stable region and the value of the critical delay as a function of κ. Note, however, that the envelope cannot be calculated in closed form for large M_X and M_v due to the algebraic complexity of (A.20). Still, the envelope can be visualized by the plot and the smallest (critical) delay is given by the case $j = 0$. The figure also indicates that as the orders M_X and M_v are increased, the envelope of the stability boundaries of the PDDE converge to that of the DDE model (see the dashed line given by (A.9)). The convergence is proven by noticing that $B_X, B_v \to \cos k - 1$ and $A_X, A_v \to \sin k$ as $M_X, M_v \to \infty$, which reduces (A.20) to (A.12). Although the convergence of the stability boundaries does not necessarily imply the convergence of solutions, Fig. 9 shows that low order models are already able to capture string (in)stability and produce realistic simulation results.

References

Avedisov, S.S., Bansal, G., Kiss, A.K., Orosz, G., 2018. Experimental verification platform for connected vehicle networks. In: Proceedings of the 21st IEEE International Conference on Intelligent Transportation Systems. Maui, HI, USA, pp. 818–823.

Avedisov, S.S., Bansal, G., Orosz, G., 2020. Impacts of connected automated vehicles on freeway traffic patterns at different penetration levels. IEEE Trans. Intell. Transp. Syst. published online.

Aw, A., Klar, A., Rascle, M., Materne, T., 2002. Derivation of continuum traffic flow models from microscopic follow-the-leader models. SIAM J. Appl. Math. 63 (1), 259–278.

Aw, A., Rascle, M., 2000. Resurrection of "second order" models of traffic flow. SIAM J. Appl. Math. 60 (3), 916–938.

Bekiaris-Liberis, N., Delis, A.I., 2020. PDE-based feedback control of freeway traffic flow via time-gap manipulation of ACC-equipped vehicles. IEEE Trans. Control Syst. Technol. 1–9.

Berg, P., Mason, A., Woods, A., 2000. Continuum approach to car-following models. Phys. Rev. E 61 (2), 1056–1066.

Besselink, B., Johansson, K.H., 2017. String stability and a delay-based spacing policy for vehicle platoons subject to disturbances. IEEE Trans. Automat. Control 62 (9), 4376–4391.

Burger, M., Göttlich, S., Jung, T., 2018. Derivation of a first order traffic flow model of Lighthill-Whitham-Richards type. In: Proceedings of the 15th IFAC Symposium on Control in Transportation Systems, Vol. 51. pp. 49–54.

Burger, M., Göttlich, S., Jung, T., 2019. Derivation of second order traffic flow models with time delays. Netw. Heterog. Media 14 (2), 265–288.

Čičić, M., Johansson, K.H., 2018. Traffic regulation via individually controlled automated vehicles: a cell transmission model approach. In: Proceedings of the 21st International Conference on Intelligent Transportation Systems. Maui, HI, USA, pp. 766–771.

Claudel, C.G., Bayen, A.M., 2010a. Lax-Hopf based incorporation of internal boundary conditions into Hamilton-Jacobi Equation. Part I: Theory. IEEE Trans. Automat. Control 55 (5), 1142–1157.

Claudel, C.G., Bayen, A.M., 2010b. Lax-Hopf based incorporation of internal boundary conditions into Hamilton-Jacobi Equation. Part II: Computational methods. IEEE Trans. Automat. Control 55 (5), 1158–1174.

Cui, S., Seibold, B., Stern, R., Work, D.B., 2017. Stabilizing traffic flow via a single autonomous vehicle: Possibilities and limitations. In: Proceedings of the 2017 IEEE Intelligent Vehicles Symposium. Los Angeles, CA, USA, pp. 1336–1341.

Daganzo, C.F., 1994. The cell transmission model: A dynamic representation of highway traffic consistent with the hydrodynamic theory. Transp. Res. B 28 (4), 269–287.

Daganzo, C.F., 2006. On the variational theory of traffic flow: Well-posedness, duality and applications. Netw. Heterog. Media 1 (4), 601–619.

Delle Monache, M.L., Liard, T., Piccoli, B., Stern, R., Work, D., 2019a. Traffic reconstruction using autonomous vehicles. SIAM J. Appl. Math. 79 (5), 1748–1767.

Delle Monache, M.L., Sprinkle, J., Vasudevan, R., Work, D., 2019b. Autonomous vehicles: From vehicular control to traffic control. In: Proceedings of the 58th IEEE Conference on Decision and Control. Nice, France, pp. 4680–4696.

Dollar, R.A., Vahidi, A., 2018. Efficient and collision-free anticipative cruise control in randomly mixed strings. IEEE Trans. Intell. Veh. 3 (4), 439–452.

Ersal, T., Kolmanovsky, I., Masoud, N., Ozay, N., Scruggs, J., Vasudevan, R., Orosz, G., 2020. Connected and automated road vehicles: state of the art and future challenges. Veh. Syst. Dyn. 58 (5), 672–704.

Feng, S., Zhang, Y., Li, S.E., Cao, Z., Liu, H.X., Li, L., 2019. String stability for vehicular platoon control: Definitions and analysis methods. Annu. Rev. Control 47, 81–97.

Garavello, M., Piccoli, B., 2006. Traffic flow on a road network using the Aw-Rascle model. Comm. Partial Differential Equations 31 (2), 243–275.

Ge, J.I., Avedisov, S.S., He, C.R., Qin, W.B., Sadeghpour, M., Orosz, G., 2018. Experimental validation of connected automated vehicle design among human-driven vehicles. Transp. Res. C 91, 335–352.

Ge, J.I., Orosz, G., 2017. Optimal control of connected vehicle systems with communication delay and driver reaction time. IEEE Trans. Intell. Transp. Syst. 18 (8), 2056–2070.

Göttlich, S., Iacomini, E., Jung, T., 2020. Properties of the LWR model with time delay. arXiv preprint (arXiv:2003.12090).

Hartung, F., Turi, J., 2000. Linearized stability in functional-differential equations with state-dependent delays. In: Proceedings of the International Conference on Dynamical Systems and Differential Equations. Atlanta, GA, USA, pp. 416–425.

Herrera, J.C., Bayen, A.M., 2010. Incorporation of Lagrangian measurements in freeway traffic state estimation. Transp. Res. B 44 (4), 460–481.

Herrera, J.C., Work, D.B., Herring, R., Ban, X., Jacobson, Q., Bayen, A.M., 2010. Evaluation of traffic data obtained via GPS-enabled mobile phones: The mobile century field experiment. Transp. Res. C 18 (4), 568–583.
Igarashi, Y., Itoh, K., Nakanishi, K., Ogura, K., Yokokawa, K., 2001. Bifurcation phenomena in the optimal velocity model for traffic flow. Phys. Rev. E 64 (4), 047102.
Jamshidnejad, A., De Schutter, B., 2015. Estimation of the generalised average traffic speed based on microscopic measurements. Transportmetrica A 11 (6), 525–546.
Jiang, L., Molnár, T.G., Orosz, G., 2021. On the deployment of V2X roadside units for traffic prediction. Transp. Res. C submitted for publication.
Jin, W.-L., 2016. On the equivalence between continuum and car-following models of traffic flow. Transp. Res. B 93 (A), 543–559.
Jin, L., Čičić, M., Amin, S., Johansson, K.H., 2018. Modeling the impact of vehicle platooning on highway congestion: A fluid queuing approach. In: Proceedings of the 21st International Conference on Hybrid Systems: Computation and Control. ACM Press, Porto, Portugal, pp. 237–246.
Kamal, M.A.S., Hayakawa, T., Imura, J., 2018. Road-speed profile for enhanced perception of traffic conditions in a partially connected vehicle environment. IEEE Trans. Veh. Technol. 67 (8), 6824–6837.
Karafyllis, I., Papageorgiou, M., 2018. Feedback control of scalar conservation laws with application to density control in freeways by means of variable speed limits. Automatica 105, 228–236.
Kreidieh, A.R., Wu, C., Bayen, A.M., 2018. Dissipating stop-and-go waves in closed and open networks via deep reinforcement learning. In: Proceedings of the 21st International Conference on Intelligent Transportation Systems. Maui, HI, USA, pp. 1475–1480.
Laval, J.A., Leclercq, L., 2013. The Hamilton-Jacobi partial differential equation and the three representations of traffic flow. Transp. Res. B 52, 17–30.
Leclercq, L., Laval, J., 2009. A multiclass car-following rule based on the LWR model. In: Traffic and Granular Flow '07 Part I. Springer, pp. 151–160.
Leclercq, L., Laval, J., Chevallier, E., 2007. The Lagrangian coordinates and what it means for first order traffic flow models. In: Proceedings of the 17th International Symposium on Transportation and Traffic Theory. pp. 735–753.
Lighthill, M.J., Whitham, G.B., 1955. On kinematic waves II. A theory of traffic flow on long crowded roads. Proc. R. Soc. A 229 (1178), 317–345.
Loumiotis, I., Demestichas, K., Adamopoulou, E., Kosmides, P., Asthenopoulos, V., Sykas, E., 2018. Road traffic prediction using artificial neural networks. In: Proceedings of the South-Eastern European Design Automation, Computer Engineering, Computer Networks and Society Media Conference. Kastoria, Greece, pp. 1–5.
Mehran, B., Kuwahara, M., Naznin, F., 2011. Implementing kinematic wave theory to reconstruct vehicle trajectories from fixed and probe sensor data. In: Proceedings of the 19th International Symposium on Transportation and Traffic Theory, Vol. 17. pp. 247–268.
Min, W., Wynter, L., 2011. Real-time road traffic prediction with spatio-temporal correlations. Transp. Res. C 19 (4), 606–616.
Molnár, T.G., Qin, W.B., Insperger, T., Orosz, G., 2018. Application of predictor feedback to compensate time delays in connected cruise control. IEEE Trans. Intell. Transp. Syst. 19 (2), 545–559.
Molnár, T.G., Upadhyay, D., Hopka, M., Van Nieuwstadt, M., Orosz, G., 2019. Lagrangian models for controlling large-scale heterogeneous traffic. In: Proceedings of the 58th IEEE Conference on Decision and Control. Nice, France, pp. 3152–3157.
Newell, G.F., 1961. Nonlinear effects in the dynamics of car following. Oper. Res. 9 (2), 209–229.
Newell, G.F., 1993. A simplified theory of kinematic waves in highway traffic, part i: General theory. Transp. Res. B 27 (4), 281–287.
Newell, G.F., 2002. A simplified car-following theory: a lower order model. Transp. Res. B 36 (3), 195–205.
Ngoduy, D., 2014. Generalized macroscopic traffic model with time delay. Nonlinear Dynam. 77 (1–2), 289–296.
Orosz, G., Ge, J.I., He, C.R., Avedisov, S.S., Qin, W.B., Zhang, L., 2017. Seeing beyond the line of site – controlling connected automated vehicles. ASME Mech. Eng. Mag. 139 (12), S8–S12.
Orosz, G., Wilson, R.E., Stépán, G., 2010. Traffic jams: dynamics and control. Phil. Trans. R. Soc. A 368 (1928), 4455–4479.
Pasquale, C., Sacone, S., Siri, S., 2018. Closed-loop stability of freeway traffic systems with ramp metering control. In: Proceedings of the 57th IEEE Conference on Decision and Control. Miami, FL, USA, pp. 223–228.
Piacentini, G., Čičić, M., Ferrara, A., Johansson, K.H., 2019. VACS equipped vehicles for congestion dissipation in multi-class CTM framework. In: Proceedings of the 18th European Control Conference. Naples, Italy, pp. 2203–2208.
Piacentini, G., Goatin, P., Ferrara, A., 2018. Traffic control via moving bottleneck of coordinated vehicles. IFAC-PapersOnLine 51 (9), 13–18.
Ploeg, J., van de Wouw, N., Nijmeijer, H., 2014. $\mathcal{L}_p$ String stability of cascaded systems: Application to vehicle platooning. IEEE Trans. Control Syst. Technol. 22 (2), 786–793.
Press, W.H., Teukolsky, S.A., Vetterling, W.T., Flannery, B.P., 1992. Numerical recipes in C: The art of scientific computing. Cambridge University Press, New York.
Qin, W.B., Orosz, G., 2019. Experimental validation on connected cruise control with flexible connectivity topologies. IEEE/ASME Trans. Mechatronics 24 (6), 2791–2802.
Richards, P.I., 1956. Shock waves on the highway. Oper. Res. 4 (1), 42–51.
Spiliopoulou, A., Manolis, D., Vandorou, F., Papageorgiou, M., 2018. Adaptive cruise control operation for improved motorway traffic flow. Transp. Res. Rec. 2672 (22), 24–35.
Stern, R.E., Cui, S., Delle Monache, M.L., Bhadani, R., Bunting, M., Churchill, M., Hamilton, N., Haulcy, R., Pohlmann, H., Wu, F., Piccoli, B., Seibold, B., Sprinkle, J., Work, D.B., 2018. Dissipation of stop-and-go waves via control of autonomous vehicles: Field experiments. Transp. Res. C 89, 205–221.
Swaroop, D., Hedrick, J.K., 1996. String stability of interconnected systems. IEEE Trans. Automat. Control 41 (3), 349–357.
Tordeux, A., Costeseque, G., Herty, M., Seyfried, A., 2018. From traffic and pedestrian follow-the-leader models with reaction time to first order convection-diffusion flow models. SIAM J. Appl. Math. 78 (1), 63–79.
van Wageningen-Kessels, F., van Lint, H., Hoogendoorn, S.P., Vuik, K., 2010. Lagrangian formulation of multiclass kinematic wave model. Transp. Res. Rec. 2188 (1), 29–36.
van Wageningen-Kessels, F., Yuan, Y., Hoogendoorn, S.P., van Lint, H., Vuik, K., 2013. Discontinuities in the Lagrangian formulation of the kinematic wave model. Transp. Res. C 34, 148–161.
Work, D.B., Bayen, A.M., 2008. Impacts of the mobile internet on transportation cyberphysical systems: Traffic monitoring using smartphones. In: Proceedings of the National Workshop for Research on High-Confidence Transportation Cyber-Physical Systems: Automotive, Aviation and Rail. Washington, DC, USA.
Work, D.B., Blandin, S., Tossavainen, O.-P., Piccoli, B., Bayen, A.M., 2010. A traffic model for velocity data assimilation. Appl. Math. Res. eXpress 2010 (1), 1–35.
Work, D.B., Tossavainen, O.-P., Blandin, S., Bayen, A.M., Iwuchukwu, T., Tracton, K., 2008. An ensemble Kalman filtering approach to highway traffic estimation using GPS enabled mobile devices. In: Proceedings of the 47th IEEE Conference on Decision and Control. Cancun, Mexico, pp. 5062–5068.
Work, D.B., Tossavainen, O.-P., Jacobson, Q., Bayen, A.M., 2009. Lagrangian sensing: Traffic estimation with mobile devices. In: Proceedings of the American Control Conference. St. Louis, MO, USA, pp. 1536–1543.
Wu, C., Bayen, A.M., Mehta, A., 2018. Stabilizing traffic with autonomous vehicles. In: Proceedings of the 2018 IEEE International Conference on Robotics and Automation. Brisbane, Australia, pp. 1–7.
Wu, C., Kreidieh, A., Parvate, K., Vinitsky, E., Bayen, A.M., 2017. Flow: Architecture and benchmarking for reinforcement learning in traffic control. arXiv preprint (arXiv:1710.05465).
Yin, D., Chen, T., Li, J., Li, K., 2018. Road traffic prediction based on base station location data by Random Forest. In: Proceedings of the 3rd International Conference on Communication and Electronics Systems. Coimbatore, India, pp. 264–270.

Yu, H., Gan, Q., Bayen, A., Krstic, M., 2020. PDE traffic observer validated on freeway data. IEEE Trans. Control Syst. Technol. 1–13.
Yu, H., Koga, S., Krstic, M., 2018. Stabilization of traffic flow with a leading autonomous vehicle. In: Proceedings of the ASME Dynamic Systems and Control Conference. no. DSCC2018–9239. Atlanta, GA, USA.
Yu, H., Krstic, M., 2019. Traffic congestion control for Aw-Rascle-Zhang model. Automatica 100, 38–51.
Yuan, Y., Van Lint, H., Van Wageningen-Kessels, F., Hoogendoorn, S., 2014. Network-wide traffic state estimation using loop detector and floating car data. J. Intell. Transp. Syst. 18 (1), 41–50.
Yuan, Y., van Lint, J.W.C., Wilson, R.E., van Wageningen-Kessels, F., Hoogendoorn, S.P., 2012. Real-time Lagrangian traffic state estimator for freeways. IEEE Trans. Intell. Transp. Syst. 13 (1), 59–70.
Zhang, H.M., 2002. A non-equilibrium traffic model devoid of gas-like behavior. Transp. Res. B 36 (3), 275–290.
Zhang, L., Orosz, G., 2016. Motif-based design for connected vehicle systems in presence of heterogeneous connectivity structures and time delays. IEEE Trans. Intell. Transp. Syst. 17 (6), 1638–1651.
Zheng, Y., Wang, J., Li, K., 2020. Smoothing traffic flow via control of autonomous vehicles. IEEE Internet Things J. 7 (5), 3882–3896.